Gunnar Bollmark

Density Matrix Renormalization Group approach to anisotropic 3-dimensional bosons

UPPSALA
UNIVERSITET

Abstract

The microscopic origin of electron pairing in Unconventional Superconductivity (USC) and in particular for USC at high critical temperature remains one of the great challenges in condensed matter physics. One large difficulty lies in the numerical simulation of such theoretical systems which are hypothesized to exhibit USC. In particular, there is still contention as to what is the ground state of the 2D Hubbard model, believed to represent USC in cuprates. As a result it is difficult to predict which systems showing USC have high critical temperatures. The related 1D Hubbard ladder does allow for high-quality, quasi-exact solutions using the Density Matrix Renormalization Group (DMRG) algorithm, and repulsively mediated electron pairing is known to occur. However, despite the appearance of such pairing these ladders cannot exhibit USC as quantum fluctuations in 1D are too strong even at zero temperature to allow for spontaneous breaking of a continuous symmetry (Mermin-Wagner theorem). Curing this deficiency can be done by connecting the 1D system to a reservoir and in particular letting the reservoir be an infinite array of such 1D systems. In this licentiate a method named MPS+MF, which utilizes DMRG and mean field theory, has been developed for solving such systems. The low-energy sector of Hubbard ladders can be realized by a Bose-Hubbard model with hard-core restrictions. Such a system is itself interesting due to its possibility of being simulated with an ultra-cold atomic gas. The validity of MPS+MF is tested against the established gold standard of Quantum Monte Carlo (QMC) which has no issues in hard-core boson systems. It is found that MPS+MF obtains a first order quantum phase transition from a 3D superfluid (SF) to a largely one-dimensional array of 1D charge-density waves (CDWs) when interaction strength is tuned which occurs at the same level as QMC. Furthermore, critical temperatures for the onset of superfluidity in the system are found to be substantially improved from full mean field approaches. Additionally, the deviation that does occur seems independent of microscopic parameters. The results show dimensional cross-over being particularly pronounced around the SF-CDW transition, verifying the approachs validity further.

List of papers

This thesis is based on the following papers, which are referred to in the text by their Roman numerals.

I Dimensional crossover and phase transitions in coupled chains: Density matrix renormalization group results.
Gunnar Bollmark, Nicolas Laflorencie, and Adrian Kantian
Phys. Rev. B 102, 195145 (2020)

Reprints were made with permission from the publishers.

Contents

List of Figures

1. Introduction

Superconductivity has over the course of history provided many challenges since its discovery in 1911 [1]. Notably, the first microscopic theory of so called conventional superconductors by Bardeen, Cooper and Schrieffer (BCS theory) was only developed over four decades after the initial discovery of the phenomenon [2]. While conventional superconductivity is largely understood through the BCS theory, examples that were not possible to explain in this manner were inevitably discovered. The first material identified to exhibit so called unconventional superconductivity (USC, or non-BCS superconductivity) was $CeCu_2Si_2$ tighly followed by the organic superconductors [3, 4, 5]. To this day unresolved issues remain such as what the pairing mechanism of electrons in so called unconventional superconductors is. Tied to this problem is that of high critical temperature (T_c) superconductors. Most high-T_c materials that have been found are of a USC type (with exceptions like the pressurized Hydrides [6, 7]) yet it remains difficult to predict whether a material exhibits USC and further whether it may obtain a large T_c [3]. This presents the issue of how to systematically predict high-T_c materials.

Historically, the two-dimensional (2D) Hubbard model has provided a minimal model containing short-range repulsive electron interactions, something which is central for USC. Due to its reasonable fidelity in representing the CuO_2 sheets in cuprates the 2D Hubbard model with on-site repulsive interactions has been hypothesized to achieve superconductivity at levels of doping close to unit filling thereby capturing the experimental findings in the high-T_c materials [8]. Despite concentrated efforts to determine whether this is true it has remained an open problem with numerous results in favor and against the hypothesis [9, 10]. In fact, the 2D Hubbard model achieves so much of the physics observed in cuprates that it is plausible that at least some variation is able to describe superconductivity [11].

While providing a starting point in the search for high T_c superconductivity the numerical and analytical difficulty in resolving the 2D Hubbard model motivates the search for other candidates. If it turns out the Hubbard model is insufficient for superconductivity the correct model would likely only become more complex, exacerbating the existing numerical issues. One alternate candidate is that of quasi one-dimensional (Q1D) systems, i.e., three-dimensional (3D) arrays of weakly coupled 1D systems. There are numerous actively researched materials of this structure such as BPCB [12], the organic

Bechgaard and Fabre salts [13], and strontium-based telephone number compounds [14, 15] which can all be made to enter an USC state. Interestingly, the organics' (Bechgaard and Fabre salts) discovery as USC materials pre-dates that of cuprates and is one of the first class of materials to defy description by BCS theory [16].

Notably, Q1D systems can be studied by several methods. Where other high T_c candidates of higher dimension may be solved with e.g. Quantum Monte Carlo (QMC) [17, 18] methods or Dynamical Mean-Field Theory (DMFT) [19], 1D and, by extension, Q1D systems are supported by additional tools. In 1D, for numerical calculations there is the possibility of Density Matrix Renormalization Group (DMRG), a highly effective algorithm which has proven markedly useful for 1D systems [20, 21, 22]. In addition, 1D allows the usage of bosonization: An effective analytical tool in 1D which often can be used to find expressions for relevant correlators of the model [23]. Furthermore, Q1D systems are readily studied in ultra-cold atom gas experiments, providing a direct experimental comparison to the theoretical approaches.

Q1D systems are of further interest as they have been known to exhibit so called dimensional crossover, i.e., when quantum coherence between lower-dimensional subsets of the system lose connection to each other and the system behaves as a set of lower-dimensional systems rather than a connected higher-dimensional system. The aforementioned organics are examples of materials which have been known to show this phenomenon [13]. Dimensional crossover may also occur across a phase transition: something which becomes very useful studying USC states. This is due to the lower-dimensional side of the phase transition being simpler to treat and may allow approximations that are imprecise in higher dimensions.

While neither repulsively mediated electron pairing nor superconductivity can occur in true 1D (i.e. 1D systems with no extent in any other dimension) the pairing has been shown to appear in the so called Hubbard ladder. This is a 1D system with one lattice site of length in an extra-dimensional direction and macroscopic length in the other (visualized in Fig. 1.1) which does exhibit repulsively mediated electron pairing [13]. Further, it is possible to use qualitative methods like mean field (MF) or renormalization group theory to show that a 3D connected set of such ladders enter an USC state, thus exhibiting dimensional crossover. The end result is an exactly solvable model based on first principles exhibiting an USC state in which the microscopic origin of the pairing mechanism is well understood from a theoretical standpoint [23, 24].

Interestingly, while 1D systems cannot by themselves attain superconductivity their 1D nature seem to provide great conditions for superconductors to achieve high critical temperatures [25]. Notably, systems of higher dimension often have their critical temperature bounded by the pairing energy of fermions. However, for materials with strong lower-dimensional properties

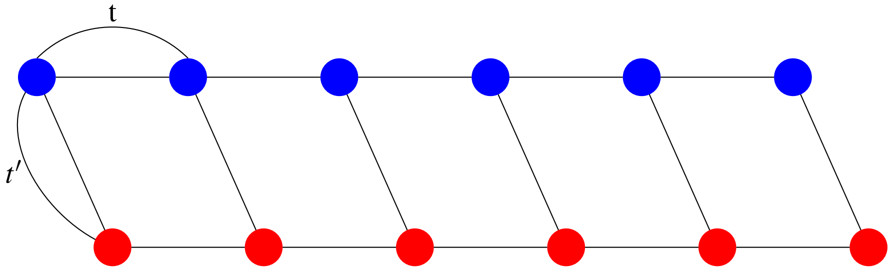

Figure 1.1. The geometry of the 1D Hubbard ladder.

the phase stiffness of the system becomes important [26]. Thus, we can imagine creating a system with large phase stiffness such that critical temperature is bounded by a pairing energy. In this manner, given a system with strong phase stiffness the strategy becomes to maximize pairing energy in order to maximize critical temperature. Previous studies indicate that pairing energies at about $0.1t$ can be achieved (where $t \sim 10^4$K is hopping strength) [24].

With this in mind, we aim to create a framework capable of high precision calculations on Q1D systems with the end goal of producing models for materials that can exhibit high-T_c superconductivity in which the microscopic origin of pairing is understood.

This licentiate

In this licentiate we study how MF theory can be used to turn a Q1D model composed of an infinite array of 1D chains coupled together weakly into an effectively 1D model. The effective 1D model is subsequently solved using DMRG, e.g., using the matrix product state (MPS) implementation thereof (see Chapter 3). We create a framework, named MPS+MF, which solves such an effective 1D system repeatedly in order to self-consistently determine the MF parameters for the effective 1D model.

While the main goal of our research is to obtain quantitatively accurate calculations of Q1D high-T_c superconductors it is of interest to test the fidelity of our results against established methods. This will be important due to the necessary inclusion of qualitative methods like MF theory. However, studying repulsively mediated electron pairing can be difficult using methods like QMC due to the fermionic sign problem [27]. Models with bosonic particles are comparatively easy to access with QMC and we begin our study using such models. In this system we study the condensate of bosonic particles which form at low temperatures and repulsion.

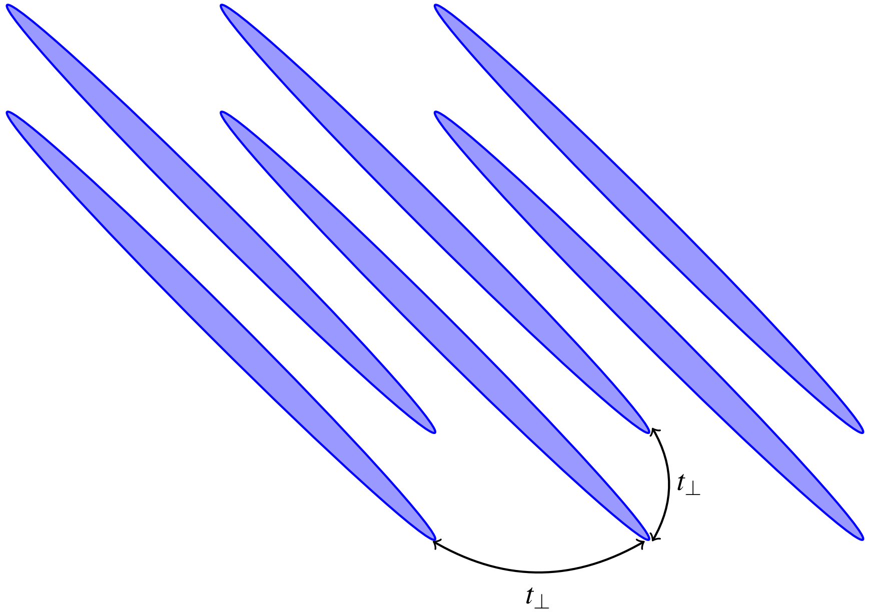

Figure 1.2. 3D anisotropic Bose-Hubbard model. Each tube represents a one-dimensional Bose-Hubbard system. The transverse hopping parameter $t_\perp$ connects the 1D systems.

Using hard-core constraints (i.e. only one boson per lattice site) this modeling can be shown to have an equivalent low-energy theory to studying attractively interacting fermions [23]. This may be interpreted as fermionic particles bound together and moving around in pairs. As such we restrict our study to two cases: bosons with hard-core restrictions and the case where no such restrictions are applied which we call soft-core bosons.

Additionally, bosonic alternatives exhibit many of the physical effects that we would also expect from an attractively interacting fermionic system. In particular, dimensional crossover has been shown to occur in bosonic systems [28, 29]. Further, using bosonic particles makes comparison with ultracold atom gas experiments more accessible [30, 31].

The work presented in this licentiate regards a 3D Bose-Hubbard model with anisotropic hopping strength and repulsive interactions along the direction of strong hopping shown in Fig. 1.2. The nature of ground states and thermal states of a self-consistent 1D Hamiltonian are analyzed. The phase transitions that occur in these models for varying interaction strengths and temperature are localized and compared to corresponding results of QMC.

We find that our results compare impressively to QMC with regards to zero-temperature quantum phase transitions which occur at almost the same level of interaction in the two methods and which furthermore agree on the transition order. In addition, we find the MPS+MF critical temperature deviating from the QMC one less than a what a full MF treatment would yield. The relative deviation we do find, while somewhat notable, seems to be approximately universal for varying microscopic parameters.

2. Ordered states

An ordered system typically has correlated behavior, i.e., when particles move and interact in a way that correlates with other particles. There are many examples of ordered states such as (anti-)ferromagnetism, superconductivity, and superfluidity. In this section we explain the concepts related to order and phase transitions necessary to understand the results of paper I.

2.1 Order

When considering phase transitions between ordered and disordered states (or between different ordered states) it is possible to define a so-called order parameter [32]. The order parameter quantifies the degree to which the system is ordered. Notably, the physical meaning of the order parameter represents the type of order a system exhibits.

An order parameter is associated with the breaking of a symmetry. A disordered system is described by macroscopic quantities like volume, particle number, and internal energy. When a system attains a certain order additional macroscopic quantities are required to determine the state of the system. For instance, the Heisenberg model (in 2 or larger dimensions)

$$H = -J \cdot \sum_{\langle i,j \rangle} \mathbf{s}_i \cdot \mathbf{s}_j,$$

will describe a disordered system above its Curie temperature as understood by the minimization of free energy $F = E - TS$, also called the paramagnetic state. Disorder in this case means that spins will be randomly oriented as this maximizes entropy S. Such a system will look the same under like rotations of each spin: There is rotational symmetry. However, below this temperature threshold the system spins will be inclined to align along the same spontaneously chosen random direction (assuming $J > 0$). The rotational symmetry is broken and a new macroscopic parameter

$$\mathbf{m} = \sum_i \langle \mathbf{s}_i \rangle \,,$$

called the magnetization is needed to describe the state. For a ferromagnet, magnetization is the so-called order parameter. Since the new phase is no longer invariant under a set of transformations under which it was previously invariant a set of symmetries have been broken in the transition to produce the ferromagnet.

In general, when transitioning to an ordered system some symmetry of the original Hamiltonian is broken. This coincides with the appearance of operator averages in the new phase which are not invariant under the Hamiltonian's symmetry group. These averages become the order parameters.

Connected to the properties of ordered states is the concept of long-range order. The appearance of an order parameter implies regularity in the state even at very long distance. In other words, we expect the value of a measurement at $\mathbf{x}$ will be able to provide information of the measurement at another position $\mathbf{y}$ even when $r = |\mathbf{x} - \mathbf{y}| \to \infty$. Given an operator ϕ which orders in the new phase this may be described by

$$\lim_{r \to \infty} \langle \phi(\mathbf{x}) \phi(\mathbf{y}) \rangle \to \langle \phi(\mathbf{x}) \rangle^2 .$$

2.2 Superfluid order

Superfluidity, the state of matter where a gas of bosonic particles flows without viscosity, is an ordered system. It can be likened to Bose-Einstein condensation (BEC) in which a macroscopic number of identical particles "condense" to the same quantum state (often, but not always, the zero momentum state). The difference between these two phases is that BEC theory assumes weak interaction while the prototypical cases of superfluidity in ^{4}He are examples of strong interactions. The properties of a superfluid can nevertheless be achieved by assuming a macroscopic population of a single state being described by a so called macroscopic wavefunction.

One method to obtain the formulation of macroscopic wavefunctions is with the use of coherent states defined by

$$|\alpha_{\mathbf{k}_0} \alpha_{\mathbf{k}_1} \ldots \rangle = e^{-\sum_{\{\mathbf{k}_i\}} |\alpha_{\mathbf{k}_i}|^2/2} \exp\left(\sum_{\{\mathbf{k}_i\}} \alpha_{\mathbf{k}_i} a^\dagger_{\mathbf{k}_i} \right) |0\rangle , \tag{2.1}$$

where ladder operators $a_{\mathbf{k}}$ have been defined for each momentum mode fulfilling $\left[a_{\mathbf{k}}, a^\dagger_{\mathbf{k}'} \right] = \delta_{\mathbf{k}\mathbf{k}'}$. Coherent states have the property that a Hamiltonian which has a spectrum of such states does not conserve particle number which can be seen from the following property

$$\langle a_{\mathbf{k}_i} \rangle = \alpha_{\mathbf{k}_i} . \tag{2.2}$$

In order to find superfluid order one has to consider the single-particle density matrix

$$\rho(\mathbf{r}-\mathbf{r}') = \langle \psi^\dagger(\mathbf{r})\psi(\mathbf{r}')\rangle = \frac{1}{V}\sum_{\mathbf{k}} e^{-i\mathbf{k}\cdot(\mathbf{r}-\mathbf{r}')}\langle a^\dagger_{\mathbf{k}} a_{\mathbf{k}}\rangle, \tag{2.3}$$

where

$$\psi(\mathbf{r}) = \frac{1}{\sqrt{V}}\sum_{\mathbf{k}} e^{i\mathbf{k}\cdot\mathbf{r}} a_{\mathbf{k}}. \tag{2.4}$$

Assuming that one momentum mode (labeled $\mathbf{k}_0$) is macroscopically occupied with N_{mac} particles we obtain

$$\langle a^\dagger_{\mathbf{k}} a_{\mathbf{k}}\rangle = n_{\mathbf{k}} = N_{mac}\delta_{\mathbf{k}\mathbf{k}_0} + f(\mathbf{k}). \tag{2.5}$$

If $f(\mathbf{k})$ is a smooth enough function we obtain in the thermodynamic limit:

$$\rho(\mathbf{r}-\mathbf{r}') = n_{mac} + \underbrace{\frac{1}{V}\int d^3\mathbf{k} e^{i\mathbf{k}\cdot(\mathbf{r}-\mathbf{r}')} f(\mathbf{k})}_{\to 0} \to n_{mac}, \tag{2.6}$$

where $n_{mac} = N_{mac}/V$ is the density of momentum mode $\mathbf{k}_0$. Further, we would expect the operators $\psi(\mathbf{r})$ to become disconnected at infinite separation $\mathbf{r}-\mathbf{r}'$. This yields another view of the single-particle density matrix

$$n_{mac} = \langle \psi^\dagger(\mathbf{r})\psi(\mathbf{r}')\rangle \approx \langle \psi^\dagger(\mathbf{r})\rangle\langle \psi(\mathbf{r}')\rangle. \tag{2.7}$$

Due to the assumption of coherent states the averages $\langle\psi(\mathbf{r})\rangle$ can be non-zero. A number-conserving state would yield a contradiction at this point in which n_{mac} would approach zero despite being required to correspond to a large fraction of total particle number. Notably, this is a type of long-range order since operators remain correlated even at infinite separation. In this case the operators are different and as such the phenomenon is called off-diagonal long-range order.

Since the average $\langle\psi(\mathbf{r})\rangle$ is related to the macroscopic population of the $\mathbf{k}_0$ state it invites the interpretation as an order parameter: When the particle number of any mode grows to macroscopic levels $\langle\psi(\mathbf{r})\rangle$ attains a finite value. Thus, superfluidity entails macroscopic populations of a mode which yields finite measurements of $\langle\psi(\mathbf{r})\rangle$. Additionally, it is worthwhile to note that $\psi(\mathbf{r})$ may be taken for a discrete lattice as well in which similar relations are obtained with the order parameter becoming the lattice site annihilation operator average:

$$n_{mac} = \langle a^\dagger_i a_j\rangle = \langle a^\dagger_i\rangle\langle a_j\rangle, \tag{2.8}$$

where i, j label two far separated positions.

2.3 Mott insulator

Mott insulators are a class of materials that insulate despite their electron structure suggesting otherwise given band theoretical calculations [33, 34]. This is proposed to be due to electron-electron interactions pinning the electrons to the atoms of the material.

In theory, such a material is simple to produce: Consider the ground-state of the spin-less 1D Fermi-Hubbard Hamiltonian which may be computed analytically

$$H_{FH} = -t\sum_i \left(c_i^\dagger c_{i+1} + \text{h.c.}\right) + V\sum_i n_i n_{i+1}. \tag{2.9}$$

Such a Hamiltonian will at half filling and sufficiently large V open a gap in the energy band [23]. The effect is that electrons can no longer move and are instead pinned to every other lattice site, driving the system into an insulating state. Adding particles to this state will cost a finite amount of energy in the thermodynamic limit: This energy difference between ground state and the state with an added particle is commonly referred to as the charge gap.

The ingredient required to produce this effect is sufficient repulsion between particles at filling fractions of the lattice which are commensurate with the interaction. Similar examples of pinning can be produced with spinful fermions where the repulsion may be on-site in addition to longer-range interactions. For such examples filling fractions are required to be unit filling for on-site interactions and lower density for longer-range interactions. Notably, the spinless fermion model described by eq. (2.9) is connected to spin-$1/2$ models via a Jordan-Wigner transformation which in turn are connected to hard-core bosons. Thus, we know that all of these examples will exhibit the Mott insulator phase.

The order parameter for a Mott insulator (fermionic/bosonic) can be expressed by the long-range order of the density-density correlator:

$$C_{zz} = \frac{1}{L}\sum_i \left(\langle n_i n_{i+r}\rangle - \langle n_i\rangle\langle n_{i+r}\rangle\right), \tag{2.10}$$

where r is a range chosen such that the correlator $\langle n_i n_{i+r}\rangle$ has converged to a constant. Notably, this expression is directly related to the S_z-S_z correlator for spin Hamiltonians and thus is similar to the anti-ferromagnetic order parameter. This expression can be generalized to longer-range repulsive interactions. Consider, the Hamiltonian in Eq. (2.9) with added next-to-nearest neighbour repulsion

$$H_{FH,nn} = H_{FH} + V'\sum_i n_{i+2} n_i. \tag{2.11}$$

If the filling is tuned to one third of the lattice size fermions may now avoid the energy penalty associated with nearest neighbour interaction by being pinned to every third site. An order parameter for this case could be defined via

$$C_{zz} = \frac{1}{L}\sum_i (-1)^{r \text{ mod } 3} \left(\langle n_i n_{i+r} \rangle - \langle n_i \rangle \langle n_{i+r} \rangle \right). \tag{2.12}$$

Similarly, for longer range interactions the order parameter would become:

$$C_{zz} = \frac{1}{L}\sum_i (-1)^{r \text{ mod } (d+1)} \left(\langle n_i n_{i+r} \rangle - \langle n_i \rangle \langle n_{i+r} \rangle \right), \tag{2.13}$$

where d is the range of interaction which pins the particles, e.g., $d = 1$ for nearest neighbour interactions and $d = 2$ for next-to-nearest range.

For the case of the Hamiltonian in Eq. (2.9): Weak enough repulsions will not be able to localize the particles and the system will behave like a Tomonaga-Luttinger liquid (see Chapter 4. In higher dimensions the low-energy behaviour will be a Fermi liquid). Such a phase is ungapped. Since the Mott insulator appears at a certain value of $U/t = U_c/t$, opening the charge gap, we obtain a phase transition between a phase with no gap and one with a gap. In addition to the order parameter, the phase transition is marked with the opening of a charge gap which can be used to mark its incidence.

3. Computational Methods

At the center of a multitude of many-body physics problems lies the many-body problem: that the total Hilbert space of solutions scales exponentially with system size. When exact analytical methods are unavailable an exponentially large Hilbert space becomes difficult to treat due to the exponentially increasing size of computational resources needed to simulate the system.

A common class of algorithms are the QMC methods. The strength and flexibility of such approaches is attested by a multitude of concrete implementations of QMC, such as the Worm algorithm [35, 36], Diagrammatic QMC [36], SSE [37]. Simultaneously, since QMC is an algorithm which samples a space of solutions it is able to run parallelized on a computing cluster with communication between computation nodes making the number of Monte Carlo updates scale almost linearly with the number of compute cores available. Unfortunately, many physical problems give rise to the so called fermionic sign problem in QMC [27]. When the physical situation is such that this occurs the computational cost to obtain reasonably low statistical errors increases exponentially with the inverse temperature making simulations, especially of ground state properties, difficult if not impossible [11, 27].

3.1 Density Matrix Renormalization Group

While QMC is a powerful method its limitations motivate the usage of additional algorithms. One such alternative is the DMRG algorithm which was developed in 1992 by Steven White [20, 21]. Intensive research has been performed on the DMRG algorithm resulting in many variations and formulations which are designed to be efficient in specific use cases, e.g., time evolution, ground state searches and exotic lattice geometries [38, 39, 40, 41].

DMRG was originally formulated in an iDMRG setting (infinite DMRG) inspired by the Numerical Renormalization Group (NRG) pioneered by Wilson [42]. The failure of NRG, specifically for real-space problems, was related to imposing artificial boundary conditions between system blocks [43]. This motivated the search for an algorithm which could embed the iterated sub-system in an environment which would be the correct surrounding at final iteration. Steven White formulated a procedure in which a linear growth of the system is performed and its minimal energy is computed in an environment which is grown at each iteration. One of the large differences between NRG and DMRG was that the former grows exponentially by finding the minimal energy of the current system connected to itself and the latter finds the minimal energy of a small sub-system in connection with a linearly growing environment.

For the purposes of this project a formulation of DMRG in a context of Matrix Product States (MPS) is used [22, 44, 45, 46]. This formulation provides a framework which is less complex than the original DMRG while still providing the same wave function solutions [47, 48, 49].

3.2 Matrix Product States

A common strategy for solving the many-body problem is to provide an ansatz for the ground state parametrized by some set of parameters. The result will be a class of states which cover a sub-set of the total Hilbert space of solutions. Thus, a less complex problem can be solved provided that the ground state can be captured sufficiently by the ansatz. Matrix product states are an example of one such ansätze, parametrized by the sizes of matrices. In fact, the parametrization of a MPS allows coverage of the entire solution Hilbert space with the caveat of intractable numerical cost.

In this section we develop the concept of a matrix product state and note key properties that make their usage natural for DMRG.

3.2.1 Schmidt decomposition

In order to connect a general quantum state to an MPS first consider the singular value decomposition (SVD) of a matrix M of dimension $N_A \times N_B$:

$$M = USV^\dagger,$$

where the properties of a SVD guarantee that

- U is of dimension $N_A \times \min(N_A, N_B)$ and $U^\dagger U = I$
- S is of dimension $\min(N_A, N_B) \times \min(N_A, N_B)$ and is diagonal. The diagonal values are called the singular values of M.
- $V^\dagger$ is of dimension $\min(N_A, N_B) \times N_B$ and $VV^\dagger = I$.

In the case of a bipartite lattice composed of two sublattices A and B it is possible to define a pure state

$$|\psi\rangle = \sum_{ij} \psi_{ij} |i\rangle_A |j\rangle_B, \tag{3.1}$$

where $\{|i\rangle_A\}$, $\{|j\rangle_B\}$ are orthonormal bases of sublattice A and B respectively. Using SVD on the components ψ_{ij} yields

$$|\psi\rangle = \sum_{ija} U_{i,a} S_{aa} (V^\dagger)_{aj} |i\rangle_A |j\rangle_B = \sum_a s_a |a\rangle_A |a\rangle_B, \tag{3.2}$$

where

$$\begin{aligned} |a\rangle_A &= \sum_i U_{i,a} |i\rangle_A \\ |a\rangle_B &= \sum_j (V^\dagger)_{a,j} |j\rangle_B . \end{aligned}$$

Equation Eq. (3.2) is a so-called Schmidt decomposition of the state $|\psi\rangle$.

Assuming that the singular values s_i are ordered such that $s_i > s_j,\ i < j$ (i.e. descending order) an optimal approximation of a matrix M can be defined in the context of SVDs:

$$M_{approx} = U S_{approx} V^\dagger, \tag{3.3}$$

$$S_{approx} = \operatorname{diag}\{s_1, s_2, \ldots, s_{min}, 0, \ldots\}, \tag{3.4}$$

where s_{min} is the smallest singular value kept and the rest are set to zero [22]. Similarly, we may truncate the singular values in Eq. (3.2) to obtain an optimal approximation of the state given a number of singular values. Using just one singular value would produce a product state i.e. an outer product of all states on A with all those on B:

$$|\psi\rangle \approx s_1 \left(\sum_i U_{i,1} |i\rangle_A \right) \otimes \left(\sum_j (V^\dagger)_{1,j} |j\rangle_B \right), \tag{3.5}$$

which yields a state in which states on sublattice A and B are completely disentangled. Notably, increasing the number of included singular values immediately yields some entanglement between sublattice states which increases as more singular values are included.

3.2.2 Fully decomposed state

Making use of the Schmidt decomposition from the previous section we are able to perform SVDs on anything that can be shaped into a matrix. A general quantum state on a 1-dimensional lattice of length L can be defined by

$$|\psi\rangle = \sum_{\{\sigma_i\}} c_{\sigma_1,\ldots,\sigma_L} |\sigma_1,\ldots,\sigma_L\rangle\,, \tag{3.6}$$

where σ_i is the quantum number on site i. The many-body problem can be found in this description in the d^L components of $c_{\sigma_1,\ldots,\sigma_L}$ (where d is the local Hilbert space dimension). It is possible to restructure these components into matrices and perform SVDs:

$$c_{\sigma_1,(\sigma_2\sigma_3\ldots\sigma_L)} = \sum_{a_1} U_{\sigma_1,a_1} S_{a_1,a_1} (V^\dagger)_{a_1,\sigma_2,\ldots,\sigma_L} = \sum_{a_1} A^{\sigma_1}_{1,a_1} c_{(a_1\sigma_2),(\sigma_3,\ldots,\sigma_L)}, \tag{3.7}$$

where A has the same components as U but has been reshaped into a set of vectors A^{σ_1} whose entries are matrices, i.e. A is a tensor of rank 3, and S,V has been absorbed into the new tensor c. In the final equality we thus obtain a reduced number of entangled components d^{L-1}. The structure chosen for the new c allows further SVDs to be performed:

$$c_{\sigma_1,(\sigma_2\sigma_3\ldots\sigma_L)} = \sum_{a_1} A^{\sigma_1}_{1,a_1} \sum_{a_2} U_{(a_1\sigma_2),a_2} S_{a_2,a_2} (V^\dagger)_{a_2,(\sigma_3,\ldots,\sigma_L)} =$$

$$\sum_{a_1} A^{\sigma_1}_{1,a_1} \sum_{a_2} A^{\sigma_2}_{a_1,a_2} c_{(a_2\sigma_3),(\sigma_4,\ldots,\sigma_L)} = \sum_{\{a_i\}} A^{\sigma_1}_{1,a_1} A^{\sigma_2}_{a_1,a_2} \cdots A^{\sigma_{L-1}}_{a_{L-2},a_{L-1}} A^{\sigma_L}_{a_{L-1},1}, \tag{3.8}$$

which can be rewritten into a matrix product

$$c_{\sigma_1,\sigma_2,\ldots,\sigma_L} = A^{\sigma_1} A^{\sigma_2} \cdots A^{\sigma_{L-1}} A^{\sigma_L}. \tag{3.9}$$

This yields the aptly named matrix product state whose basis state weights are determined by a product of matrices:

$$|\psi\rangle = \sum_{\{\sigma_i\}} A^{\sigma_1} A^{\sigma_2} \cdots A^{\sigma_{L-1}} A^{\sigma_L} |\sigma_1,\ldots,\sigma_L\rangle\,. \tag{3.10}$$

Note that the first and final set of matrices, A^{σ_1} and A^{σ_L}, are row and column vectors respectively, i.e. the matrix entries are size $1 \times d$ and $d \times 1$. The many-body complexity has been hidden away in the size of these matrices which increase toward some maximum at the matrix product center (i.e. at $A^{\sigma_{L/2}}$). The properties of SVD yield matrix dimensions of A in Eq. (3.10): $(1 \times d)$, $(d \times d^2)$, $(d^2 \times d^3)\ldots$ where d is the local Hilbert space dimension. The matrix sizes become unmanageable even for quite short systems such that a cut-off, χ, must be introduced in accordance with the optimal approximation Eq. (3.3). The resultant matrix size is commonly referred to as the bond dimension.

It shall often be practical to represent states like eq. (3.10) schematically as the amount of indices and sums to be aware of increases strongly, especially as operators are included. A typical way to do this is shown in Figure 3.1. The

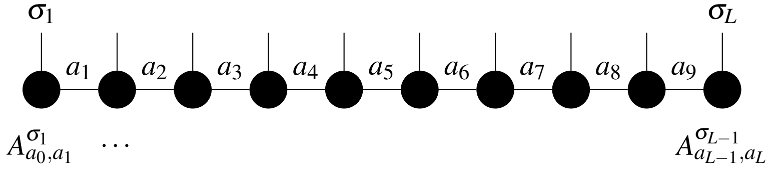

Figure 3.1. A schematic representation of the MPS where a_0 and a_L are dummy indices of dimensions 1.

free legs represent physical indices $\{\sigma_i\}$ which may be contracted with other MPS. The connecting legs represent the matrix or bond indices which connect each dot, representing the matrices in the MPS, to the next.

3.2.3 MPS properties

Granted that the left matrices of a SVD, U, fulfill the condition $U^\dagger U = I$ the constructed A tensors must in turn fulfill the correspondent equation:

$$\delta_{a'_i,a_i} = \sum_{a_{i-1},\sigma_i} (U^\dagger)_{a'_i,(a_{i-1}\sigma_i)} U_{(a_{i-1}\sigma_i),a_i} = \sum_{a_{i-1},\sigma_i} (A^{\sigma_i\dagger})_{a'_i,a_{i-1}} A^{\sigma_i}_{a_{i-1},a_i} \tag{3.11}$$

$$\implies \sum_{\sigma_i} A^{\sigma_i\dagger} A^{\sigma_i} = I. \tag{3.12}$$

It is important to note that the converse is not necessarily true i.e.

$$\sum_{\sigma_i} A^{\sigma_i} A^{\sigma_i\dagger} = ? \tag{3.13}$$

Such matrices are said to be left-normalized. The corresponding MPS in Eq. (3.10) is as such called a left-canonical MPS. It is also possible to divide up the tensor components c by starting from the right and constructing matrices from V instead of from U. This leads to a state which has the same appearance as Eq. (3.10):

$$|\psi\rangle = \sum_{\{\sigma_i\}} B^{\sigma_1} B^{\sigma_2} \cdots B^{\sigma_{L-1}} B^{\sigma_L} |\sigma_1, \ldots, \sigma_L\rangle, \tag{3.14}$$

where B is obtained by reshaping $V^\dagger$. The crucial difference between the two states is in the normalization condition:

$$\delta_{a'_i,a_i} = \sum_{a_{i-1},\sigma_i} (V^\dagger)_{a'_i,(a_{i-1}\sigma_i)} V_{(a_{i-1}\sigma_i),a_i} = \sum_{a_{i-1},\sigma_i} B^{\sigma_i}_{a'_i,a_{i-1}} (B^{\sigma_i\dagger})_{a_{i-1},a_i} \tag{3.15}$$

$$\implies \sum_{\sigma_i} B^{\sigma_i} B^{\sigma_i\dagger} = I. \tag{3.16}$$

Matrices which fulfill this condition are referred to as being right-normalized. Thus, Eq. (3.14) is called a right-canonical MPS. Due to the usefulness of the identity relations a SVD brings to a state both Eq. (3.10) and (3.14) are used in DMRG in favour of other MPS structures where no such normalization condition can be identified.

Further, it is possible to define MPS which are in a so-called mixed canonical state. If the procedure performed in Eq. (3.14) is done only partially and the remaining tensor components are created using Eq. (3.10) the MPS will have both A and B matrices. Such states are of the form

$$|\psi\rangle = \sum_{\{\sigma_i\}} A^{\sigma_1} A^{\sigma_2} \cdots A^{\sigma_l} \Lambda^{[l]} B^{\sigma_{l+1}} \cdots B^{\sigma_{L-1}} B^{\sigma_L} |\sigma_1, \ldots, \sigma_L\rangle, \tag{3.17}$$

where $\Lambda^{[l]}$ is a diagonal matrix containing the singular values of a SVD performed at site l.

3.2.4 Matrix Product Operator

It is also possible to express general operators in the form of a matrix product. Any operator can be defined by

$$O = \sum_{\{\sigma,\sigma'\}} O^{\sigma_1',\sigma_2',\ldots,\sigma_L'}_{\sigma_1,\sigma_2,\ldots,\sigma_L} |\sigma_1, \sigma_2, \ldots, \sigma_L\rangle \langle \sigma_1', \sigma_2', \ldots, \sigma_L'| . \tag{3.18}$$

Once again using SVD it is possible to divide the operator components into matrices. Note the extra set of physical degrees of freedom σ'. Grouping each σ_i together yields

$$\begin{aligned} O &= \sum_{\{\sigma,\sigma'\}} O^{(\sigma_1\sigma_1'),(\sigma_2\sigma_2'\cdots\sigma_L\sigma_L')} |\sigma_1, \sigma_2, \ldots, \sigma_L\rangle \langle \sigma_1', \sigma_2', \ldots, \sigma_L'| \\ &= \sum_{\{\sigma,\sigma'\}} W^{\sigma_1,\sigma_1'} O^{\sigma_2,\sigma_2',\ldots,\sigma_L,\sigma_L'} |\sigma_1, \sigma_2, \ldots, \sigma_L\rangle \langle \sigma_1', \sigma_2', \ldots, \sigma_L'|, \end{aligned} \tag{3.19}$$

where a similar splitting of indices was performed as was done for MPS. Note that $W^{\sigma_1\sigma_1'}$ is a row vector. Continuing this process for each pair of σ_i, σ_i' we obtain

$$O = \sum_{\{\sigma,\sigma'\}} W^{\sigma_1,\sigma_1'} W^{\sigma_2,\sigma_2'} \cdots W^{\sigma_L,\sigma_L'} |\sigma_1, \sigma_2, \ldots, \sigma_L\rangle \langle \sigma_1', \sigma_2', \ldots, \sigma_L'| . \tag{3.20}$$

Similar to the case of MPS a schematic representation of operators may be performed as shown in Figure 3.2.

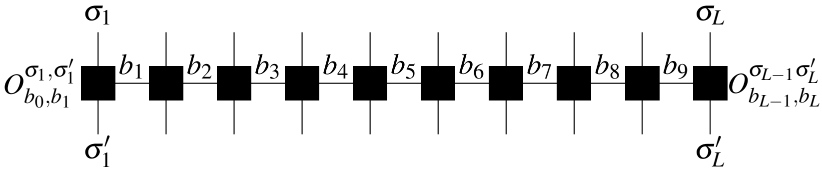

Figure 3.2. A schematic representation of a MPO.

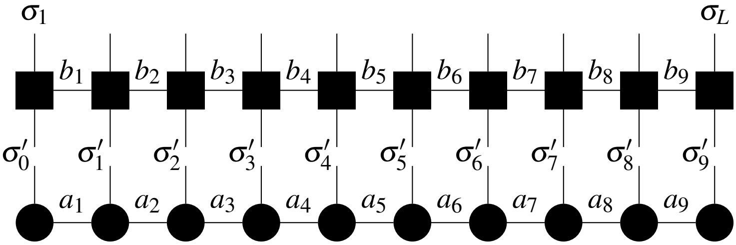

Figure 3.3. Schematic representation of an MPO applied to an MPS.

This description makes it easier to describe the application of operators to MPS. Consider a MPS which has mixed left and right-normalized matrices M. The application of the operator given in Eq. (3.20) to such a state becomes

$$\begin{aligned} O|\psi\rangle = & \\ & \sum_{\{\sigma,\sigma'\}} W^{\sigma_1,\sigma'_1} W^{\sigma_2,\sigma'_2} \dots W^{\sigma_L,\sigma'_L} M^{\sigma'_1} M^{\sigma'_2} \dots M^{\sigma'_{L-1}} M^{\sigma'_L} \left|\sigma_1,\sigma_2,\dots,\sigma_L\right\rangle \\ & = \sum_{\{\sigma\}} N^{\sigma_1} N^{\sigma_2} \cdots N^{\sigma_{L-1}} N^{\sigma_L} \left|\sigma_1,\sigma_2,\dots,\sigma_L\right\rangle, \end{aligned} \tag{3.21}$$

where

$$N^{\sigma_i}_{(a_{i-1}b_{i-1}),(a_i b_i)} = \begin{cases} \sum_{\sigma'_1} W^{\sigma_1\sigma'_1}_{1,b_1} M^{\sigma'_1}_{1,a_1} \text{ if i=1} \\ \\ \sum_{\sigma'_1} W^{\sigma_L\sigma'_L}_{b_{L-1},1} M^{\sigma'_L}_{a_{L-1},1} \text{ if i=L} \\ \\ \sum_{\sigma'_i} W^{\sigma_i\sigma'_i}_{b_{i-1},b_i} M^{\sigma'_i}_{a_{i-1},a_i} \text{ otherwise.} \end{cases} \tag{3.22}$$

Notably, the structure of the MPS is preserved by the MPO application and the result is that the MPS bond dimension is inflated by the MPO bond dimension. The contraction of an MPO with an MPS can be visualized in the schematic notation using Figures. 3.1 and 3.2 as shown in Fig. 3.3.

3.3 Finite size DMRG

DMRG can be used to study different physical situations. For the purposes of this research project we need both ground states and thermal states and will formulate them in a finite size DMRG algorithm.

3.3.1 Ground state DMRG

To obtain the ground state of a system the energy of a MPS trial state must be minimized. The most efficient way to perform this minimization is a variational search in the space of possible MPS given a maximally allowed bond dimension, χ [22]. The energy is defined by

$$E = \frac{\langle\psi|H|\psi\rangle}{\langle\psi|\psi\rangle}. \tag{3.23}$$

Let M denote the MPS matrices of $|\psi\rangle$. The state norm becomes

$$\langle\psi|\psi\rangle = \sum_{\{\sigma\}} \left(M^{\sigma_L\dagger} M^{\sigma_{L-1}\dagger} \cdots M^{\sigma_2\dagger} M^{\sigma_1\dagger}\right) \times \left(M^{\sigma_1} M^{\sigma_2} \cdots M^{\sigma_{L-1}} M^{\sigma_L}\right). \tag{3.24}$$

Since minimizing with respect to the entire set of matrices is an exponentially difficult problem the strategy is to minimize locally at some pair of sites (or alternatively at a single site). Restructuring the state norm to reflect this we obtain:

$$\begin{aligned}
\langle\psi|\psi\rangle &= \sum_{\{\sigma\}} \left(B^{\sigma_L\dagger} B^{\sigma_{L-1}\dagger} \cdots A^{\sigma_2\dagger} A^{\sigma_1\dagger}\right) \times \left(A^{\sigma_1} A^{\sigma_2} \cdots B^{\sigma_{L-1}} B^{\sigma_L}\right) \\
&= \sum_{\{\sigma\}} \sum_{\{a_l\}} \sum_{\{a'_l\}} \left(A^{\sigma_{l-1}\dagger} A^{\sigma_{l-2}\dagger} \cdots A^{\sigma_1\dagger} A^{\sigma_1} \cdots A^{\sigma_{l-2}} A^{\sigma_{l-1}}\right)_{a_{l-1},a'_{l-1}} \times \\
&\qquad \left(B^{\sigma_{l+1}} B^{\sigma_{l+2}} \cdots B^{\sigma_L} B^{\sigma_L\dagger} \cdots B^{\sigma_{l+3}\dagger} B^{\sigma_{l+2}\dagger}\right)_{a'_{l+1}a_{l+1}} \times \\
&\qquad\qquad M^{\sigma_l *}_{a_{l-1}a_l} M^{\sigma_l}_{a'_{l-1}a'_l} M^{\sigma_{l+1} *}_{a_l a_{l+1}} M^{\sigma_{l+1}}_{a'_l a'_{l+1}} = \\
&\sum_{\sigma_l} \sum_{\{a_l\}} \sum_{\{a'_l\}} \Psi^A_{a_{l-1}a'_{l-1}} \Psi^B_{a'_{l+1}a_{l+1}} M^{\sigma_l *}_{a_{l-1}a_l} M^{\sigma_l}_{a'_{l-1}a'_l} M^{\sigma_{l+1} *}_{a_l a_{l+1}} M^{\sigma_{l+1}}_{a'_l a'_{l+1}}.
\end{aligned} \tag{3.25}$$

It is possible to construct $|\psi\rangle$ in a mixed-canonical representation such that left of index l the state is left-canonical and right of site $l+1$ it is right-canonical. This has the benefit of simplifying the overlap tremendously due to left- and right-normalization

$$\Psi^A_{a_{l-1}a'_{l-1}} = \delta_{a_{l-1}a'_{l-1}} \tag{3.26}$$

$$\Psi^B_{a'_{l+1}a_{l+1}} = \delta_{a'_{l+1}a_{l+1}}. \tag{3.27}$$

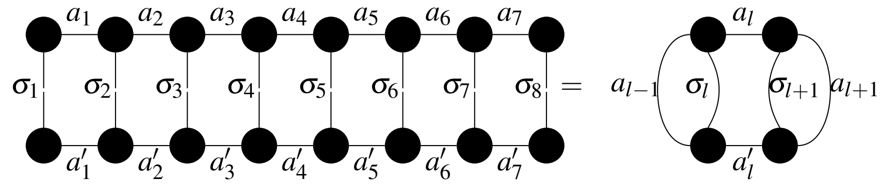

Figure 3.4. A schematic representation of the state norm in Eq. (3.25) simplified in accordance with Eq. (3.26).

In fact, this can be neatly expressed in the schematic notation defined in Figs. 3.1-3.3. The contraction from Eq. (3.25) can be described as shown in Fig. 3.4. From this it can clearly be seen that the norm of a properly prepared state in accordance with Eq. (3.26) is computationally cheap to obtain.

In addition to the state norm we need the energy expectation value. It becomes

$$\begin{aligned}\langle\psi|H|\psi\rangle = \sum_{\{\sigma,\sigma'\}} &\left(M^{\sigma_L\dagger}M^{\sigma_{L-1}\dagger}\cdots M^{\sigma_2\dagger}M^{\sigma_1\dagger}\right)\times \\ &W^{\sigma_1,\sigma'_1}W^{\sigma_2,\sigma'_2}\ldots W^{\sigma_L,\sigma'_L}\times\left(M^{\sigma'_1}M^{\sigma'_2}\cdots M^{\sigma'_{L-1}}M^{\sigma'_L}\right) \\ = \sum_{\{\sigma,\sigma'\}}\sum_{\{a,a',b\}} &\left(M^{\sigma_1*}_{1,a_1}W^{\sigma_1,\sigma'_1}_{1,b_1}M^{\sigma'_1}_{1,a'_1}\right)\times\left(M^{\sigma_2*}_{a_1,a_2}W^{\sigma_2,\sigma'_2}_{b_1,b_2}M^{\sigma'_2}_{a'_1,a'_2}\right)\cdots \\ \times &\left(M^{\sigma_l*}_{a_{l-1},a_l}W^{\sigma_l,\sigma'_l}_{b_{l-1},b_l}M^{\sigma'_l}_{a'_{l-1},a'_l}\right)\cdots\times\left(M^{\sigma_L*}_{a_{L-1},1}W^{\sigma_L,\sigma'_L}_{b_{L-1},1}M^{\sigma'_L}_{a'_{L-1},1}\right). \qquad (3.28)\end{aligned}$$

Each bracket treats a specific site in the finite lattice. It is now possible to isolate a specific pair of sites l and $l+1$ in an environment of the remaining lattice:

$$\begin{aligned}\langle\psi|H|\psi\rangle = &\sum_{\{\sigma_l\sigma'_l\}}\sum_{\{b_l\}}\sum_{\{a_l\}}\sum_{\{a'_l\}}L_{a_{l-1},a'_{l-1},b_{l-1}}\times \\ \times &\left(M^{\sigma_l*}_{a_{l-1},a_l}W^{\sigma_l,\sigma'_l}_{b_{l-1},b_l}M^{\sigma'_l}_{a'_{l-1},a'_l}\right)\left(M^{\sigma_{l+1}*}_{a_l,a_{l+1}}W^{\sigma_{l+1},\sigma'_{l+1}}_{b_l,b_{l+1}}M^{\sigma'_{l+1}}_{a'_l,a'_{l+1}}\right)R_{a_{l+1},a'_{l+1},b_{l+1}}, \qquad (3.29)\end{aligned}$$

where

$$\begin{aligned}L_{a_{l-1},a'_{l-1},b_{l-1}} = &\sum_{\sigma_1,\ldots,\sigma_{l-2}}\sum_{a_1,\ldots,a_{l-2}}\sum_{b_1\ldots,b_{l-2}}\sum_{a'_1\ldots,a'_{l-2}}\left(M^{\sigma_1*}_{1,a_1}W^{\sigma_1,\sigma'_1}_{1,b_1}M^{\sigma'_1}_{1,a'_1}\right)\times \\ \times &\left(M^{\sigma_2*}_{a_1,a_2}W^{\sigma_2,\sigma'_2}_{b_1,b_2}M^{\sigma'_2}_{a'_1,a'_2}\right)\cdots\times\left(M^{\sigma_{l-1}*}_{a_{l-2},a_{l-1}}W^{\sigma_{l-1},\sigma'_{l-1}}_{b_{l-2},b_{l-1}}M^{\sigma'_{l-1}}_{a'_{l-2},a'_{l-1}}\right) \qquad (3.30)\end{aligned}$$

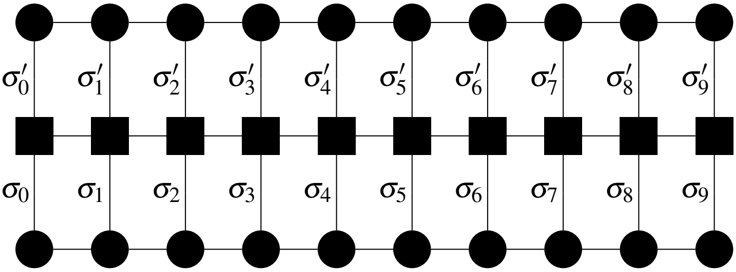

Figure 3.5. A schematic representation of the energy expectation value.

$$\begin{aligned} R_{a_{l+1},a'_{l+1},b_{l+1}} &= \\ &\sum_{\sigma_{l+1},\dots,\sigma_L} \sum_{a_{l+1},\dots,a_L} \sum_{b_{l+1}\dots,b_L} \sum_{a'_{l+1}\dots,a'_L} \left(M^{\sigma_{l+2}*}_{a_{l+1},a_{l+2}} W^{\sigma_{l+2},\sigma'_{l+2}}_{b_{l+1},b_{l+2}} M^{\sigma'_{l+2}}_{a'_{l+1},a'_{l+2}} \right) \times \\ &\cdots \times \left(M^{\sigma_{L-1}*}_{a_{L-2},a_{L-1}} W^{\sigma_{L-1},\sigma'_{L-1}}_{b_{L-2},b_{L-1}} M^{\sigma'_{L-1}}_{a'_{L-2},a'_{L-1}} \right) \left(M^{\sigma_L*}_{a_{L-1},1} W^{\sigma_L,\sigma'_L}_{b_{L-1},1} M^{\sigma'_L}_{a'_{L-1},1} \right), \quad (3.31) \end{aligned}$$

are the left and right partitions around a site pair $(l, l+1)$ of the lattice. It is worthwhile to note that partitioning the matrices in this manner can be done for any site pair. The expectation value Eq. (3.29) is schematically represented in Fig. 3.5. Notably, the contraction for each σ_l does not simplify as in Fig. 3.4.

The central MPS matrices may be multiplied together and defined as a new matrix

$$\left(M^{\sigma_l*}_{a_{l-1},a_l} M^{\sigma_{l+1}*}_{a_l,a_{l+1}} \right) = \left(\Theta^{\sigma_l\sigma_{l+1}}_{a_{l-1}a_{l+1}} \right)^* \qquad (3.32)$$

We next minimize $\langle\psi|H|\psi\rangle$ with respect to the components of $\left(\Theta^{\sigma_l\sigma_{l+1}}_{a_{l-1}a_{l+1}} \right)^*$ (i.e. the components of the two matrices at l) by looking for an extremum which yields the equation

$$\begin{aligned} &\sum_{\sigma'_l\sigma'_{l+1}} \sum_{\{b_l\}} \sum_{\{a_l\}} L_{a_{l-1},a'_{l-1},b_{l-1}} \left(W^{\sigma_l,\sigma'_l}_{b_{l-1},b_l} W^{\sigma_{l+1},\sigma'_{l+1}}_{b_l,b_{l+1}} \Theta^{\sigma_l\sigma_{l+1}}_{a'_{l-1}a'_{l+1}} \right) R_{a_{l+1},a'_{l+1},b_{l+1}} \\ &\qquad - E_{loc} \sum_{a'_l a'_{l-1}} \Psi^A_{a_{l-1}a'_{l-1}} \Psi^B_{a'_{l+1}a_{l+1}} \Theta^{\sigma_l\sigma_{l+1}}_{a'_{l-1}a'_{l+1}} = 0, \quad (3.33) \end{aligned}$$

where E_{loc} denotes the energy of the system (dependent on the local choice of Θ). This equation can be reshaped into an eigenvalue problem with the form

$$Hv - E_{loc} Pv = 0, \qquad (3.34)$$

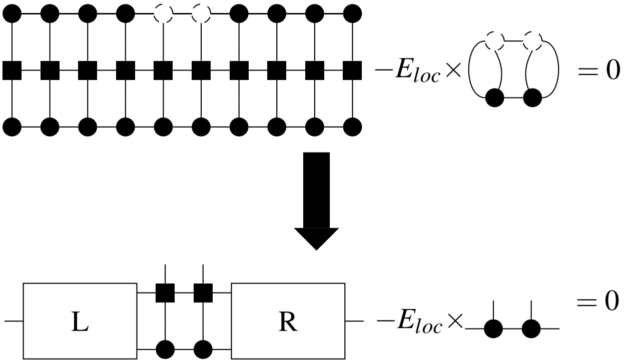

Figure 3.6. A schematic representation of Eq. 3.33. Dashed circles indicate the objects which have been eliminated through derivation.

with the following definitions

$$H_{(\sigma_l\sigma_{l+1}a_{l-1}a_{l+1}),(\sigma'_l\sigma'_{l+1}a'_{l-1}a'_{l+1})} = \sum_{\{b_l\}} L_{a_{l-1},a'_{l-1},b_{l-1}} W^{\sigma_l,\sigma'_l}_{b_{l-1},b_l} W^{\sigma_{l+1},\sigma'_{l+1}}_{b_l,b_{l+1}} R_{a_{l+1},a'_{l+1},b_{l+1}} \tag{3.35}$$

$$v_{(\sigma'_l\sigma'_{l+1}a'_{l-1}a'_{l+1})} = \Theta^{\sigma'_l\sigma'_{l+1}}_{a'_{l-1}a'_{l+1}} \tag{3.36}$$

$$P_{(\sigma_l\sigma_{l+1}a_{l-1}a_{l+1}),(\sigma'_l\sigma'_{l+1}a'_{l-1}a'_{l+1})} = \Psi^A_{a_{l-1}a'_{l-1}} \Psi^B_{a'_{l+1}a_{l+1}} \delta_{\sigma_l\sigma'_l}\delta_{\sigma_{l+1}\sigma'_{l+1}}. \tag{3.37}$$

Solving the equation yields a spectrum of energies corresponding to different choices of $\Theta^{\sigma_l\sigma_{l+1}}$ where we are interested in the smallest energy. Once an energy is determined the pair matrix Θ can be divided in two with an SVD.

In this manner it is possible to move through the system with SVD, changing the bi-partition location, and minimizing energy at every step. The cumbersome calculation of each contraction shown in Fig. 3.5 can be circumvented by saving the contractions as the bi-partition is moved through the system thus allowing repeated usage of already performed contractions. Thus, as can be seen in Fig. 3.6 the problem is reduced to a repeated local treatment of the state.

The process we have described is commonly referred to as two-site DMRG since at each minimization step two sites are considered at once. It is also possible to perform single-site DMRG with the same process where only one MPS matrix M is included in the Θ definition of Eq. (3.32).

3.4 Time evolution

For thermal states it is necessary to perform imaginary time evolution such that the evolved state represents the appropriate inverse temperature β. Even here the many-body problem is a source of difficulty. Generally, if the Hamiltonian H is itself time-independent a time evolution operator is given by integrating Schrödinger's equation:

$$U(t) = e^{-iHt}. \tag{3.38}$$

This operator is difficult to obtain exactly since it requires the complete diagonalization of H. Fortunately, MPS methods can be used to reduce the complexity of this problem as well.

3.4.1 Trotter decomposition

Similarly to ground state DMRG it is difficult to apply an entire MPO to an MPS immediately. Instead, applying the MPO on each bond separately allows for efficient time evolution.

Consider the time evolution operator

$$U = e^{-iH\Delta t} = \underbrace{e^{-ih_{L-1}\Delta t}}_{U_{L-1}} e^{-ih_{L-2}\Delta t} \cdots e^{-ih_2\Delta t} e^{-ih_1\Delta t} + \mathscr{O}\left(\Delta t^2\right), \tag{3.39}$$

where Δt is the amount of time to evolve, $H = \sum_i h_i$ the Hamiltonian and h_i contains all interactions acting on the bond $(i, i+1)$, assuming that H only contains nearest neighbour interactions. Eq. (3.39) is an example of a first-order Trotter decomposition where the error of order $\mathscr{O}(\Delta t^2)$ is due to the fact that in general $[h_i, h_j] \neq 0$ if $i \neq j$.

Splitting the time evolution operator allows the application thereof bond-wise as shown schematically in Fig. 3.7 with the cost of an error related to the time-step size. In addition, the issue of diagonalizing H has been partially solved since only the diagonalization of h_i separately is now required. In practice, many h_i will be the same local operator strongly reducing the time consumption of creating a time evolution operator.

When the Hamiltonian only contains nearest neighbour interactions the h_i on odd bonds commute amongst each other and similarly for even bonds. Thus, we are free to apply time evolution in any order on odd/even bonds. Evolving an amount of time now becomes equivalent to applying the time evolution on odd bonds followed by that of even bonds:

$$e^{-iH_{even}\Delta t} e^{-iH_{odd}\Delta t} \left|\psi(t)\right\rangle = \left|\psi(t+\Delta t)\right\rangle, \tag{3.40}$$

which simplifies application of the time evolution operator as is shown in Fig. 3.8.

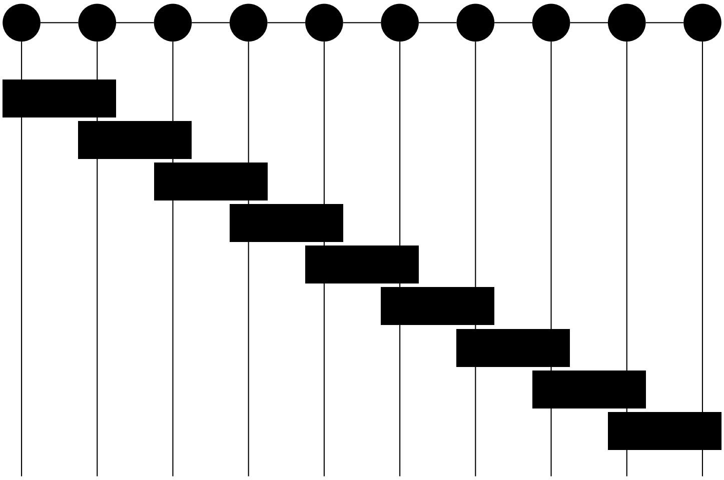

Figure 3.7. Schematic representation of an application of U in eq. (3.39) to an MPS. Note that each local operator U_i changes the MPS so that they must be applied sequentially.

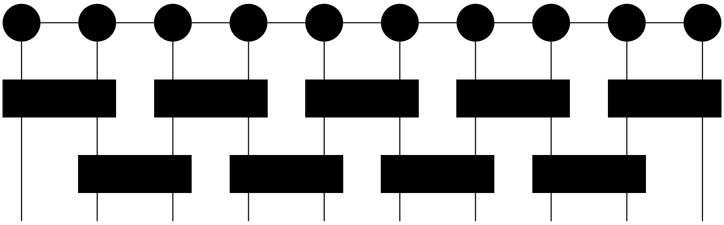

Figure 3.8. Schematic representation of eq. (3.40). With the U_i divided such that they commute amonst each other they can be applied in any order.

It is notable that higher-order Trotter decompositions can be made by dividing up the Hamiltonian such that the Δt^2 contributions cancel. A second-order Trotter decomposition can be achieved with

$$e^{-iH\Delta t} = e^{-iH_{odd}\Delta t/2} e^{-iH_{even}\Delta t} e^{-iH_{odd}\Delta t/2} + \mathscr{O}(\Delta t^3). \tag{3.41}$$

Commonly, the time step Δt will be chosen to be small so that the error related to Trotter decomposition is small. From Eq. (3.41) the H_{odd} pieces from a current and subsequent time step can be combined creating almost the exact same routine as for a first-order Trotter decomposition with a strongly reduced error.

Despite this, precision of results will often require yet a higher order of Trotter decomposition. For thermal states we shall often make use of a fourth order Trotter decomposition

$$e^{-iH\Delta t} = U(a\Delta t)U(b\Delta t)U(c\Delta t)U(b\Delta t)U(a\Delta t) \tag{3.42}$$

where

$$U(\Delta t) = e^{-iH_{odd}\Delta t/2} e^{-iH_{even}\Delta t} e^{-iH_{odd}\Delta t/2}, \tag{3.43}$$

$$a = b = \frac{1}{4-4^{1/3}}, \tag{3.44}$$

$$c = 1-2a-2b. \tag{3.45}$$

3.4.2 MPS time evolution

Assuming a state which has a bi-partition at the pair $(l, l+1)$ the appropriate evolution operator to apply here is given by

$$U_l = \left(U^{\sigma_l \sigma_{l+1}, \sigma_l' \sigma_{l+1}'} \right). \tag{3.46}$$

Combining MPS matrices as in Eq. (3.32) we may apply Eq. (3.46) such that only Θ is affect and no other part of the MPS:

$$\sum_{\{\sigma'\}} U^{\sigma_l \sigma_{l+1}, \sigma_l' \sigma_{l+1}'} \Theta^{\sigma_l' \sigma_{l+1}'}_{a_{l-1} a_{l+1}} = \Phi^{\sigma_l \sigma_{l+1}}_{a_{l-1} a_{l+1}}. \tag{3.47}$$

The resultant matrix is now subject to a SVD

$$\Phi^{\sigma_l \sigma_{l+1}}_{a_{l-1} a_{l+1}} = \sum_{a_l} U_{(a_{l-1}\sigma_l), a_l} S_{a_l a_l} (V^\dagger)_{a_l, (a_{l+1}\sigma_{l+1})}, \tag{3.48}$$

where we see an inflation of matrix size by local Hilbert space dimension d which will require truncation and limits the amount of time that can be evolved while keeping errors due to truncation small. Thus, the original shape of the MPS can be retrieved and it is possible move the bi-partition to the subsequent bond.

In practice, applying the odd time evolution will mean sweeping through the state using SVD and applying identity operators on the even bonds and conversely for the sweep back applying the even evolution. Notably, higher order Trotter decompositions require more sweeps to perform one time step and thus take more time to simulate for a given time step. However, for a given error tolerance a much larger time step can be used in higher-order Trotter decompositions compared to the lower-order alternatives leading to a potentially quicker solution.

3.4.3 Thermal states

Using time evolution it is possible to obtain thermal averages by setting the evolved time as imaginary:

$$U(-i\beta) = e^{-iH(-i\beta)} = e^{-\beta H}, \tag{3.49}$$

where the evolved time now may be interpreted as inverse temperature β. To perform thermal averages we need the thermal density matrix, ρ_β:

$$\langle O \rangle_\beta = \mathrm{Tr}\left[O\rho_\beta\right]. \tag{3.50}$$

One way to obtain this operator is via state purification [50]. Consider an auxiliary system (A) connected to the physical one (P) and a Schmidt decomposition between the two systems:

$$|\psi\rangle = \sum s_a |a\rangle_P |a\rangle_A. \tag{3.51}$$

This yields the density matrix of P as

$$\rho_P = \mathrm{Tr}_A(|\psi\rangle\langle\psi|) = \sum s_a^2 |a\rangle_P \langle a|_P. \tag{3.52}$$

The thermal density matrix is given by

$$\rho_P(\beta) = \frac{1}{Z(\beta)} e^{-\beta H\otimes I} = \frac{Z(0)}{Z(\beta)} e^{-\beta H\otimes I/2} \underbrace{\mathrm{Tr}_A(|\psi(0)\rangle\langle\psi(0)|)}_{\rho_P(0)=1/Z(0)} e^{-\beta H\otimes I/2}, \tag{3.53}$$

where $\psi(0)$ denotes an infinite temperature state (i.e. $\beta = 0$) and I denotes an identity matrix acting on a Hilbert space the size of the auxiliary system A. The imaginary time evolution operators may be moved inside the trace since $H \otimes I$ only acts as an identity in the auxiliary space:

$$\rho_P(\beta) = \frac{Z(0)}{Z(\beta)} \mathrm{Tr}_A\left(|\psi(\beta/2)\rangle\langle\psi(\beta/2)|\right). \tag{3.54}$$

Assuming that an observable O only acts in the physical sub-space P we may use this thermal density matrix such that thermal averages are obtained by expectation values:

$$\langle O\rangle_\beta = \mathrm{Tr}_P\left[O\rho_\beta\right] = \frac{Z(0)}{Z(\beta)}\mathrm{Tr}(O\left|\psi(\beta/2)\right\rangle\left\langle\psi(\beta/2)\right|) \tag{3.55}$$

The partition function, $Z(\beta)$ is given by

$$\begin{aligned} Z(\beta) = \mathrm{Tr}\left(e^{-\beta H}\right) &= Z(0)\mathrm{Tr}\left(\left|\psi(\beta/2)\right\rangle\left\langle\psi(\beta/2)\right|\right) \\ &= Z(0)\left\langle\psi(\beta/2)|\psi(\beta/2)\right\rangle, \end{aligned} \tag{3.56}$$

which finally yields the expression for thermal averages

$$\langle O\rangle_\beta = \frac{\langle\psi(\beta/2)|O|\psi(\beta/2)\rangle}{\langle\psi(\beta/2)|\psi(\beta/2)\rangle}. \tag{3.57}$$

Thus, in order to obtain a thermal average we must start with an infinite temperature state (i.e. $\beta = 0$) and perform imaginary time evolution on the state up to $\beta/2$.

It remains to compute the (purified) infinite temperature state. In the physical sub-system this will be a product state with equal amplitude for all combinations such that each site is the same i.e. the thermal density matrix is an identity. For one site (labeled by i) we obtain (assuming that all quantum number combinations are allowed)

$$\begin{aligned} \rho_{Pi}(0) = \sum_{\sigma_i}\frac{1}{d}\left|\sigma_i\right\rangle\left\langle\sigma_i\right| &= \frac{1}{d}\mathrm{Tr}_A\left[\left(\sum_{\sigma_i}\left|\sigma_i\right\rangle_P\left|\sigma_i\right\rangle_A\right)\left(\sum_{\sigma_i'}\left\langle\sigma_i'\right|_P\left\langle\sigma_i'\right|_A\right)\right] \\ &= \mathrm{Tr}_A(\left|\psi_i(0)\right\rangle\left\langle\psi_i(0)\right|), \end{aligned} \tag{3.58}$$

where we have made the identification

$$\left|\psi_i(0)\right\rangle = \sum_{\sigma_i}\frac{1}{\sqrt{d}}\left|\sigma_i\right\rangle_P\left|\sigma_i\right\rangle_A. \tag{3.59}$$

Finally, the infinite temperature state is obtained as

$$\left|\psi(0)\right\rangle = \bigotimes_{i=1}^{L}\left|\psi_i(0)\right\rangle. \tag{3.60}$$

3.5 DMRG truncation error

Whether performing time evolution or variational minimization of the energy each bi-partition of the MPS is associated with the application of some operator which inflates the bond dimension locally. In the case of time evolution the inflation is by a factor of the MPO bond dimension and for ground state searches it is the local Hilbert space dimension d.

If the new matrix size would be accepted continuing the sweep intractable matrix sizes would be obtained quickly making truncation a necessary approximation. Due to the variational nature of ground state DMRG the error due to truncation error can be treated differently between the two presented algorithms.

3.5.1 Ground state truncation error

When performing the minimization step of eq. (3.33) the eigenvalue problem solution results in a new matrix which minimizes local bond energy. When an SVD is applied the resultant bond dimension is inflated by d forcing us to truncate to the set matrix dimension χ. The result is that some number of singular values are removed from the central matrix of the SVD in accordance with eq. (3.4).

In order to quantify the error consider a given state decomposed at a given site as in eq. (3.2)

$$|\psi\rangle = \sum_{a=1}^{N} s_a |a\rangle , \tag{3.61}$$

where N is the number of singular values required to exactly describe the current bi-partition. During a truncation the bond dimension $\chi < N$ would be selected to reduce the size of the MPS:

$$|\psi_{trunc}\rangle = \sum_{a=1}^{\chi} s_a |a\rangle . \tag{3.62}$$

The expectation values of an observable O using the truncated and exact state becomes

$$\langle O\rangle = \langle\psi|O|\psi\rangle = \sum_{a}^{N}\sum_{b}^{N} s_a s_b \langle b|O|a\rangle \tag{3.63}$$

$$\langle O\rangle_{trunc} = \langle\psi_{trunc}|O|\psi_{trunc}\rangle = \sum_{a}^{\chi}\sum_{b}^{\chi} s_a s_b \langle b|O|a\rangle . \tag{3.64}$$

The expectation value error becomes

$$\begin{aligned}|\langle O\rangle - \langle O\rangle_{trunc}| &= \sum_a^N\sum_b^N s_a s_b \langle b|O|a\rangle - \sum_a^{\chi}\sum_b^{\chi} s_a s_b \langle b|O|a\rangle \\ &= \sum_{a=\chi+1}^{N}\sum_{b=1}^{\chi} s_a s_b \langle b|O|a\rangle + \sum_{a=1}^{\chi}\sum_{b=\chi+1}^{N} s_a s_b \langle b|O|a\rangle \\ &\quad + \sum_{a=\chi+1}^{N}\sum_{b=\chi+1}^{N} s_a s_b \langle b|O|a\rangle . \end{aligned} \tag{3.65}$$

It is clear that the error depends on the operator O. Since the set of density matrix eigenvectors $|a\rangle$ is orthonormal if O_{loc} is an operator which acts locally in the sense that it does not connect any of the eigenvectors:

$$\langle a|b\rangle = \delta_{ab} \implies \langle a|O_{loc}|b\rangle = \delta_{ab}\langle a|O_{loc}|a\rangle , \tag{3.66}$$

we would obtain

$$\begin{aligned}|\langle O\rangle - \langle O\rangle_{trunc}| = \sum_{a=\chi+1}^{N}\sum_{b=\chi+1}^{N} s_a s_b \langle b|O|a\rangle &= \sum_{a=\chi+1}^{N} s_a^2 \langle a|O|a\rangle \\ &\leq O_{max}\varepsilon_{\psi}, \end{aligned} \tag{3.67}$$

where $O_{max} = \max(\langle a|O_{loc}|a\rangle , \{|a\rangle\})$ and $\varepsilon_{\psi} = \sum_{a=\chi+1}^{N} s_a^2$. Thus, the measurement error at one truncation for local operators is bounded by the sum of squared discarded singular values.

However, if O is able to connect some eigenvectors the error may be larger than indicated in eq. (3.67). If O connects two eigenvectors where only one singular value is small the error would have a larger leading term

$$|\langle O\rangle - \langle O\rangle_{trunc}| \sim 2s_1 s_{\chi}. \tag{3.68}$$

Since the leading singular value s_1 is never going to be small particularly difficult operators may obtain errors which are hard to control. In particular, longer-range measurements may cause such changes, making truncation errors for such observables a common issue when using DMRG [43].

The quantity ε_{ψ} is often called the truncation error [43]. Despite the problematic error in correlation functions the truncation error proves to be useful in minimizing the error associated with truncating the bond dimension of matrices. In particular, a common observation of measurements of DMRG is that the dependence of fully converged ground-state energy error on truncation error is a linear relationship [51, 52]:

$$\frac{E_{DMRG} - E_{Exact}}{E_{Exact}} \propto \varepsilon_{\psi}. \tag{3.69}$$

Using this relationship, it is possible to obtain ground-state energies extrapolated to the $\varepsilon_\psi \to 0$ limit even if such calculations would require intractable bond dimensions to obtain otherwise.

For single-site observables (e.g. density or magnetization) the behaviour is similar to that of energy with the caveat that achievable precision is lower than that of energy [43]. Hence, precision of local quantities can typically be improved by using a similar fitting form as eq. (3.69) i.e. the infinite bond dimension (or zero truncation error) measurement of one-point correlators (in particular energy) can be approximated by extrapolation to the limit of zero truncation error.

Unfortunately, two-point correlators have no general heuristic like eq. (3.69) applicable to them and ε_ψ can not in general used for an extrapolation to zero truncation error. In this manner, the precision of two-point correlators in DMRG are reliant on how large a bond dimension can be chosen.

Notably, we have treated a single bi-partition and minimization, in this context defining the truncation error ε_ψ and it's relation to the measurement error of observables. In practice, there are several ways to define truncation error since it's main purpose is to serve as a variable to be used for extrapolation. Two common definitions are the maximal truncation error of one bi-partition and the sum of all bi-partition truncated weights in the last sweep, respectively. In both of these methods it is sufficient to know the truncation error from the last sweep since any change of the state caused by further minimization will only be possible outside the fixed bond dimension. Hence, a state which is converged given the set bond dimension will have all change brought on by minimization removed via truncation and all subsequent sweeps yields the same truncation error.

3.5.2 Time evolution truncation error

As opposed to the ground state algorithm the time evolution routine sweeps through the system repeatedly applying a single time step operator to each bond thereby evolving the state. In this manner, the truncation error is not accurately depicted by the last sweeps maximal truncation or sum since it contains only the error made by the final application of the time evolution operator. Instead, the truncation error from each sweep needs to be summed to obtain an accurate error in which it is possible to extrapolate.

4. Bosonization

For a large class of many-body systems it is a good approximation to describe low-energy physics using Fermi-liquid theory (FL). The model under consideration is described by one of free fermionic quasiparticles with renormalized mass and Fermi velocity. Thus, the problem is greatly simplified and details of interaction are considered modifications of these parameters e.g. a strong repulsion could lead to a quasiparticle with a larger effective mass. The strength of this approach is particularly apparent as dynamics outside of FL theory can be taken into account perturbatively, greatly expanding what can be computed.

However, for 1D systems the FL theory does not work as a low-energy theory. Since it relies on low-energy excitations being describable as fermionic quasiparticles, it fails when the low-energy state is not close to a free fermion description.

In 1D, a fermionic particle cannot move past an identical copy of itself. Thus, any free movement has to affect all particles that are in the path of movement, i.e., a particle must push all other particles ahead of it to move. This makes a free fermion Hamiltonian a poor description of the system. Further difficulty arises with spinful fermions where so called spin-charge separation occurs: collective charge excitations and spin excitations may propagate at different speeds causing the elementary excitation to change from one into two separate ones. This makes fermionic quasiparticles, upon which Fermi-liquid theory is built unsuitable to describe the low-energy physics of a 1D system. Instead a different type of physics called Tomonaga-Luttinger liquid (TLL) theory, based on the Tomonaga-Luttinger model, may be defined.

The first consideration of the bosonization transformation was first conceived of by Bloch in 1933 [53, 54]. After being rediscovered several times, most notably by Tomonaga [55] proving that the transformation holds in 1D, its Abelian version was solved by Luther and Peschel [56] and Mandelstam [57] independently. It's non-Abelian version was solved by Witten in 1984 [58]. As will be shown this approach allows the solution of fermionic systems with interactions. Interestingly, many of the properties that make a bosonization transformation possible do not generalize to higher dimensions rendering the method exclusive to 1D systems [54, 23].

Many reviews have been written about bosonization [54, 23, 59]. In the following sections we largely follow Giamarchi's book on Quantum Physics in One Dimension [23].

4.1 Tomonaga-Luttinger model

In many low-energy descriptions of fermions it is not uncommon to use a model with linear dispersion relation. Such a description is commonly called the Tomonaga-Luttinger model and is defined by the Hamiltonian

$$H_{TL} = \sum_{k,r=-1,1} v_F(rk - k_F)c^\dagger_{r,k}c_{r,k}, \tag{4.1}$$

where $r = -1$ ($r = 1$) is considered left-moving (right-moving) respectively which have to be defined due to the singular point in $q = 0$. A particle-hole excitation (of one particle orientation) would produce an energy difference given by

$$\Delta E = v_F(r(k+q) - k_F) - v_F(rk - k_F) = v_F rq, \tag{4.2}$$

where $sgn(q) = r$. The dependence of this particle-hole excitation is only on the exchanged momentum q. Since each such excitation has uniquely defined energy and momentum a quasi-particle theory may be formulated around them with creation operator

$$\rho^\dagger_r(q) = \sum_k c^\dagger_{r,k+q}c_{rk}. \tag{4.3}$$

For a Hamiltonian like this the vacuum state is the Dirac sea. Since the Dirac sea is filled there are an infinite number of occupied states. This raises issues when considering density operators as they count the Dirac sea states as well. To solve this we remove the background density value

$$c^\dagger_{rk}c_{rk} \to c^\dagger_{rk}c_{rk} - \langle 0|c^\dagger_{rk}c_{rk}|0\rangle \equiv : c^\dagger_{rk}c_{rk} :, \tag{4.4}$$

where $:AB:$ denotes normal ordering of operators and $|0\rangle$ is a state in which the Dirac sea is occupied. Note that the equivalence only holds if the set of operators A and B are linear combinations of the creation and annihilation operators. Thus, the density fluctuation operator in Eq. 4.3 instead becomes

$$:\rho^\dagger_r(q) := \begin{cases} \sum_k c^\dagger_{r,k+q}c_{rk} & q \neq 0 \\ N_r = \sum_k c^\dagger_{rk}c_{rk} - \langle 0|c^\dagger_{rk}c_{rk}|0\rangle & q = 0. \end{cases} \tag{4.5}$$

The commutation relations between different flavors of density operators becomes zero due to being different particles. For identical flavors we obtain (omitting the flavor index)

$$\begin{aligned} \left[\rho^\dagger(q), \rho^\dagger(-q')\right] &= \sum_{k_1k_2} c^\dagger_{k_1+q}c_{k_1}c^\dagger_{k_2-q'}c_{k_2} - c^\dagger_{k_2-q'}c_{k_2}c^\dagger_{k_1+q}c_{k_1} \\ &= \sum_{k_1k_2} c^\dagger_{k_1+q}c_{k_2}\delta_{k_1,k_2-q'} - c^\dagger_{k_2-q'}c_{k_1}\delta_{k_2,k_1+q} \\ &= \sum_{k_1} c^\dagger_{k_1+q}c_{k_1+q'} - c^\dagger_{k_1+q-q'}c_{k_1}. \end{aligned} \tag{4.6}$$

Shifting the sum in the right term by q' yields a zero commutator. However, to allow this variable change we must use normal-ordered operators:

$$
\begin{aligned}
\left[\rho^\dagger(q),\rho^\dagger(-q')\right] &= \sum_{k_1} :c^\dagger_{k_1+q}c_{k_1+q'}: - :c^\dagger_{k_1+q-q'}c_{k_1}: \\
&\quad + \sum_{k_1} \langle 0|c^\dagger_{k_1+q}c_{k_1+q'}|0\rangle - \langle 0|c^\dagger_{k_1+q-q'}c_{k_1}|0\rangle \\
&= \delta_{q,q'}\sum_{k_1} \langle 0|c^\dagger_{k_1+q}c_{k_1+q}|0\rangle - \langle 0|c^\dagger_{k_1}c_{k_1}|0\rangle\,. \qquad (4.7)
\end{aligned}
$$

Specializing to a 1D system with periodic boundary conditions such that momentum is quantized $q=\frac{2\pi n}{L}$ allows the computation of these averages leading to an approximatively bosonic commutator

$$
\left[\rho^\dagger_r(q),\rho^\dagger_{r'}(-q')\right] = -\delta_{r,r'}\delta_{q,q'}\frac{rqL}{2\pi}. \qquad (4.8)
$$

Thus, it is possible to create bosonic operators:

$$
b^\dagger_q = \sqrt{\frac{2\pi}{|q|L}}\sum_r \Theta(rq)\rho^\dagger_r(q) \qquad (4.9)
$$

$$
b_q = \sqrt{\frac{2\pi}{|q|L}}\sum_r \Theta(rq)\rho^\dagger_r(-q), \qquad (4.10)
$$

where $\Theta(x)$ is the Heaviside step function. Attempting to simply substitute these operators in eq. (4.1) does not work. Instead, we discern the Hamiltonians expressed in bosonic operators via its commutation relations:

$$
\begin{aligned}
[b_q,H_{TL}] &= \sqrt{\frac{2\pi}{|q|L}}\sum_r \Theta(rq)\sum_{k,r'} v_F(r'k-k_F)\left[\rho^\dagger_r(-q),c^\dagger_{r',k}c_{r',k}\right] \\
&= \sqrt{\frac{2\pi}{|q|L}}\sum_r \Theta(rq)\sum_{k,r'} v_F(r'k-k_F)\sum_{k'}\left(c^\dagger_{k'-q,r}c_{kr'}\delta_{kk'}\delta_{rr'} - c^\dagger_{kr'}c_{k'r}\delta_{k,k'-q}\delta_{rr'}\right) \\
&= \sqrt{\frac{2\pi}{|q|L}}\sum_r \Theta(rq)\sum_k \left(v_F(rk-k_F)-v_F(r(k-q)-k_F)\right)c^\dagger_{k-q,r}c_{kr} \\
&= v_F|q|b_q, \qquad (4.11)
\end{aligned}
$$

where $q\neq 0$. However, this commutator is consistent with a Hamiltonian

$$
H_{TL} = \sum_{p\neq 0} v_F|p|b^\dagger_p b_p, \qquad (4.12)
$$

using the bosonic commutator rules for b_q. Interestingly, while eq. (4.12) is quartic in fermionic operators its commutator agrees with that of eq. (4.1) which is quadratic in the same operators. Including the $q = 0$ piece requires taking the zero-momentum limit of eqs. (4.9) and (4.10) giving the following addition to eq. (4.12)

$$H_{TL} = \sum_{p \neq 0} v_F |p| b_p^\dagger b_p + \frac{v_F \pi}{2L} \left(\sum_r N_r \right)^2, \tag{4.13}$$

where the added term approaches zero in the thermodynamic limit.

Constructing the following field operators

$$\phi(x) = -(N_1 + N_{-1}) \frac{\pi x}{L} - \frac{i\pi}{L} \sum_{q \neq 0} \frac{1}{q} e^{-\alpha|q|/2 - iqx} \left(\rho_1^\dagger(q) + \rho_{-1}^\dagger(q) \right), \tag{4.14}$$

$$\theta(x) = (N_1 - N_{-1}) \frac{\pi x}{L} + \frac{i\pi}{L} \sum_{q \neq 0} \frac{1}{q} e^{-\alpha|q|/2 - iqx} \left(\rho_1^\dagger(q) - \rho_{-1}^\dagger(q) \right), \tag{4.15}$$

where α is a cut-off which acts like a smallest distance (or inversely, maximal momentum) of the theory allows us to re-express the Hamiltonian in a more convenient way. Consider the commutator

$$[\phi(x), \theta(y)] = i\frac{\pi}{2} \mathrm{Sign}(y - x), \tag{4.16}$$

which allows us to identify ϕ and θ as canonically conjugate field operators:

$$[\phi(x), \nabla\theta(y)] = \frac{i\pi}{2} \frac{d}{dy} (\Theta(y - x) - \Theta(x - y)) = i\pi\delta(x - y), \tag{4.17}$$

i.e. the conjugate momentum to ϕ is given by

$$\Pi(x) = \frac{1}{\pi} \theta(x). \tag{4.18}$$

Using the field operators it is possible to write the Hamiltonian as

$$H_{TL} = \int \frac{v_F}{2\pi} \left[(\pi\Pi(x))^2 + \nabla\phi(x)^2 \right] dx. \tag{4.19}$$

Notably, this is a Hamiltonian with a Gaussian action and observables can conveniently be computed using path integral formalism (see Sec. 4.2).

4.2 Tomonaga-Luttinger liquids

While the Tomonaga-Luttinger model is exactly described by the Hamiltonian in eq. (4.19) it is possible to connect it to a much more general class of models.

Considering any systems density operator at a position x

$$\rho(x) = \sum_i \delta(x - x_i), \tag{4.20}$$

where x_i are the particle positions, the 1D nature of our model allows us to unambiguously label each particle using a labeling field $\phi(x)$ which fulfills

$$\phi_{lab}(x_i) = 2\pi i. \tag{4.21}$$

The density expressed in terms of ϕ becomes

$$\rho(x) = \nabla\phi_{lab}(x) \sum_i \delta\left(\phi_{lab}(x) - 2\pi i\right) = \frac{\nabla\phi_{lab}(x)}{2\pi} \sum_p e^{ip\phi_{lab}(x)}, \tag{4.22}$$

where Poisson's formula has been used in the last equality and we have assumed that $\nabla\phi_{lab}(x) > 0$ which may be done without issue in 1D.

We now choose the labeling field as a fluctuation around the crystalline solution:

$$\phi_{lab}(x) = 2\pi\rho_0 x - 2\phi_{fluct}(x), \tag{4.23}$$

where the field ϕ_{fluct} represents this fluctuation. Inserting this definition into eq. (4.22) and setting $\phi(x) = \phi_{fluct}(x)$ yields

$$\rho(x) = \left(\rho_0 - \frac{1}{\pi}\nabla\phi(x)\right) \sum_p e^{i2p(\pi\rho_0 x - \phi(x))}. \tag{4.24}$$

From this we construct the single-particle creation (annihilation) operators

$$\psi^\dagger(x) = \rho(x)^{1/2} e^{-i\theta(x)}, \tag{4.25}$$

where θ is a phase factor operator. Using the appropriate commutation relations allows us to determine how the two fields ϕ and θ relate to each other. For a bosonic system the single-particle operators fulfill the commutation relations

$$\left[\psi(x), \psi^\dagger(x')\right] = \delta(x - x'), \tag{4.26}$$

which is fulfilled when

$$\left[\rho(x), e^{-i\theta(x')}\right] = \delta(x - x') e^{-i\theta(x')}. \tag{4.27}$$

Expanding ρ in terms of ϕ yields

$$\begin{aligned}\left[\rho(x), e^{-i\theta(x')}\right] = &\left(\rho_0 - \frac{1}{\pi}\nabla\phi(x)\right) \sum_p e^{i2p\pi\rho_0 x} \left[e^{-i2p\phi(x)}, e^{-i\theta(x')}\right] \\ &- \left[\frac{1}{\pi}\nabla\phi(x), e^{-i\theta(x')}\right] \sum_p e^{i2p(\pi\rho_0 x - \phi(x))}.\end{aligned} \tag{4.28}$$

Notably, in the continuum limit strongly oscillating factors like $e^{i2p\pi\rho_0 x}$ will approach zero. Thus, if the commutator of ϕ and θ is determined by the relation

$$\left[\frac{1}{\pi}\nabla\phi(x), \theta(x')\right] = -i\delta(x-x'), \tag{4.29}$$

then the condition for bosonic commutation relations in eq. (4.27) is fulfilled in the continuum limit. Notably, we find the fields ϕ and θ to be canonically conjugate with the canonical momentum defined by

$$\Pi(x) = \frac{1}{\pi}\nabla\theta(x). \tag{4.30}$$

The square root of a delta function in a distributional sense is given by

$$\sqrt{\delta[\varphi]} = \sqrt{-\int_{-\infty}^{\infty} \frac{d}{dx}(\varphi(x))\,\Theta(x)dx} = \sqrt{\varphi(0)} = \frac{\delta[\varphi]}{\sqrt{\varphi(0)}}, \tag{4.31}$$

where $\{\varphi\}$ is a smooth set of test functions that decay sufficiently fast. This means a square root of the Dirac delta function is itself a delta function up to a pre-factor. Using Eq. (4.25) and Eq. (4.31) the single-particle operators now become

$$\psi^\dagger(x) = \left(\rho_0 - \frac{1}{\pi}\nabla\phi(x)\right)^{1/2} \sum_p e^{i2p(\pi\rho_0 x - \phi(x))} e^{-i\theta(x)}, \tag{4.32}$$

where we used the fact that the momentum sum may be written as a delta function whose square root is equal to itself. Notably, these operators have been constructed to fulfill boson commutation relations. In order, to obtain fermions we simply replace eq. (4.27) with a fermionic anti-commutator

$$\{\psi_F(x), \psi_F^\dagger(x')\} = \delta(x-x'), \tag{4.33}$$

which can be fulfilled by adding the oscillating ϕ_{lab} field:

$$\begin{aligned}\psi_F^\dagger(x) &= \rho(x)^{1/2} e^{-i\theta(x)} e^{i\frac{\pi}{2}\phi_{lab}(x)} \\ &= \left(\rho_0 - \frac{1}{\pi}\nabla\phi(x)\right)^{1/2} \sum_p e^{i2(p+1)(\pi\rho_0 x - \phi(x))} e^{-i\theta(x)}. \end{aligned}\tag{4.34}$$

Given the usual terms in a 1D Hamiltonian such as interactions and kinetic energy we must determine how these are expressed in the field operators ϕ and θ to lowest order regardless of whether the system models fermions or bosons. Relevant operators include

- $\nabla\phi(x)^2$ as it comes from density-density interactions
- $\nabla\theta(x)^2$ as it comes from kinetic energy $\nabla\psi^\dagger\nabla\psi$.

In fact, ignoring higher order terms these two are all that will be required to describe the Hamiltonian. Cross terms are prohibited due to symmetry:

$$\begin{aligned} &\rho(x) \to \rho(-x),\ \psi^\dagger(x) \to \psi^\dagger(-x) \\ \implies &\phi(x) \to -\phi(-x),\ \theta(x) \to \theta(-x), \end{aligned}$$

which makes both $\phi\theta$ and $\nabla\phi\nabla\theta$ terms symmetry-breaking.

Thus, the low-energy properties of all 1D systems are described by the Hamiltonian

$$H_{TLL} = \frac{\hbar}{2\pi} \int dx \left[\frac{uK}{\hbar^2} \left(\pi \Pi(x)\right)^2 + \frac{u}{K} \left(\nabla\phi(x)\right)^2 \right], \tag{4.35}$$

where u and K are chosen to parametrize the constant in front of the only relevant terms in the Hamiltonian. Typically, these are difficult or impossible to obtain by analytical means but once found will determine all low-energy properties of the system.

Notably, eq. (4.35) is the same Hamiltonian as eq. (4.19) with $uK = u/K = v_F$ which places the Tomonaga-Luttinger model as the low-energy fixed point of all massless 1D systems. This model plays the same roll Fermi liquids do in higher dimensions giving rise to the name Tomonaga-Luttinger Liquid (TLL). Further, The Hamiltonian in eq. (4.35) has a Gaussian action and allows the computation of observables by use of path integral formalism.

4.3 Correlators and expectation values

In order to obtain expectation values of observables we note that all observable can be expressed in the single-particle creation and annihilation operators given in eq. (4.32). Notably, they are constructed using the conjugate field ϕ and θ. The evaluation of useful expectation value such as Green's functions or correlations we must know how to manage the following expectation values

$$\langle \phi(x_1)\phi(x_2) \rangle, \tag{4.36}$$
$$\langle \phi(x_1)\theta(x_2) \rangle, \tag{4.37}$$
$$\langle \theta(x_1)\theta(x_2) \rangle. \tag{4.38}$$

As an example, consider the density-density correlations (using eq. (4.24))

$$\begin{aligned} \langle \rho(x,\tau)\rho(0,0) \rangle = \rho_0^2 + \frac{1}{\pi^2} \langle \nabla\phi(x,\tau)\nabla\phi(0) \rangle \\ + \rho_0^2 \cos\left(2\pi\rho_0 x\right) \langle e^{i2\phi(x,\tau)} e^{i2\phi(0,0)} \rangle \\ + \rho_0^2 \cos\left(4\pi\rho_0 x\right) \langle e^{i4\phi(x,\tau)} e^{i4\phi(0,0)} \rangle + \dots, \end{aligned} \tag{4.39}$$

where the exponential expectation value can be simplified due to the quadratic Hamiltonian:

$$\langle e^{O} \rangle = e^{\frac{1}{2}\langle O^2 \rangle}, \tag{4.40}$$

where O is an operator linear in the field operators. We are left with computing

$$\langle (\phi(x,\tau) - \phi(0,0))^2 \rangle, \tag{4.41}$$

$$\langle \nabla\phi(x,\tau)\nabla\phi(0,0) \rangle. \tag{4.42}$$

Ultimately, it is only necessary to compute the two-point correlator of ϕ since the measurements are functionally the same when Fourier transformed.

Path integral formalism may be used to determine expectation values such as the one in eq. (4.41) which yields (naming $(x,\tau) = r_1$ and $(0,0) = r_2$)

$$\begin{aligned} &\langle (\phi(r_1) - \phi(r_2))^2 \rangle \\ &\quad = \frac{1}{(\beta\Omega)^2} \sum_{\mathbf{q}_1,\mathbf{q}_2} \langle \phi(\mathbf{q}_1)\phi(\mathbf{q}_2) \rangle \left(e^{i\mathbf{q}_1 r_1} - e^{i\mathbf{q}_1 r_2} \right) \left(e^{i\mathbf{q}_2 r_1} - e^{i\mathbf{q}_2 r_2} \right), \end{aligned} \tag{4.43}$$

where $\mathbf{q}_i = (k_i, \omega_{n,i}/u)$ and $r_i = (x_i, u\tau_i)$. Representing the expectation value of Fourier transformed operators with a path integral yields

$$\langle \phi(\mathbf{q}_1)\phi(\mathbf{q}_2) \rangle = \int \mathscr{D}[\phi,\theta]\, \phi(\mathbf{q}_1)\phi(\mathbf{q}_2) e^{-S}, \tag{4.44}$$

where S is the action in imaginary time of eq. (4.35) defined by

$$S = -\int_0^{\beta} d\tau \int dx \frac{1}{\pi} \nabla\theta i\partial_\tau\phi - \frac{1}{2\pi}\left[\frac{u}{K}\nabla\phi^2 + uK\nabla\theta^2 \right] \tag{4.45}$$

Fourier transforming the action yields

$$S = \frac{1}{\beta\Omega}\sum_{\mathbf{q}} \frac{ik\omega_n}{\pi}\phi(\mathbf{q})\theta(-\mathbf{q}) + \frac{uk^2}{2\pi K}\phi(\mathbf{q})\phi(-\mathbf{q}) + \frac{uKk^2}{2\pi}\theta(\mathbf{q})\theta(-\mathbf{q}). \tag{4.46}$$

Since ϕ and θ are real-valued field we may further simplify the action by defining the matrix A as follows

$$\begin{aligned} S &= \frac{1}{2}\frac{1}{\beta\Omega}\sum_{\mathbf{q}} (\theta(\mathbf{q})^*, \phi(\mathbf{q})^*) A^{-1} \begin{pmatrix} \theta(\mathbf{q}) \\ \phi(\mathbf{q}) \end{pmatrix} \\ &= \frac{1}{\beta\Omega}\sum_{\mathbf{q}} (\theta(\mathbf{q})^*, \phi(\mathbf{q})^*) \begin{pmatrix} \frac{uKk^2}{\pi} & \frac{ik\omega_n}{\pi} \\ \frac{ik\omega_n}{\pi} & \frac{uk^2}{\pi K} \end{pmatrix} \begin{pmatrix} \theta(\mathbf{q}) \\ \phi(\mathbf{q}) \end{pmatrix}. \end{aligned} \tag{4.47}$$

Finally, since the action is quadratic in the field operators it is possible to utilize Gaussian integration and a general expectation value of two-point functions becomes

$$\langle \phi_k \phi_l \rangle = \frac{\left(\prod_{i,j} \int \frac{d\phi_i d\phi_j}{2\pi i} \right) \phi_k \phi_l e^{\sum_{i,j} \phi_i^* M_{ij} \phi_j}}{\left(\prod_{i,j} \int \frac{d\phi_i d\phi_j}{2\pi i} \right) e^{\sum_{i,j} \phi_i^* M_{ij} \phi_j}} = (M^{-1})_{kl}, \tag{4.48}$$

where ϕ_i denotes any field at any co-ordinate (the derivation of eq. (4.48) is given in Appendix A.2).

Noting that the inverse of $\left(A^{-1}\right)^{-1} = A$ is given by

$$A = \frac{\pi}{k^2((uk)^2 + \omega_n^2)} \begin{pmatrix} \frac{uk^2}{K} & -ik\omega_n \\ -ik\omega_n & uKk^2 \end{pmatrix}, \tag{4.49}$$

we obtain the expectation value

$$\langle \phi(\mathbf{q}_1)\phi(\mathbf{q}_2) \rangle = \frac{\beta\Omega\delta_{-\mathbf{q}_1,\mathbf{q}_2} uK\pi}{(uk)^2 + \omega_n^2}. \tag{4.50}$$

From eq. (4.41) we now obtain

$$\langle (\phi(x,\tau) - \phi(0,0))^2 \rangle = \frac{1}{\beta\Omega} \sum_{k,\omega_n} (1 - \cos(kx + \omega_n\tau)) \frac{2uK\pi}{\omega_n^2 + (uk)^2}, \tag{4.51}$$

where the sum has been split into a momentum (k) and Matsubara frequency (ω_n) sum separately. The latter can be performed in the standard way by utilizing a pole-summation using the Bose factor [60, 61]

$$f_B(z) = \frac{1}{e^{\beta z} - 1}. \tag{4.52}$$

This leaves the momentum sum which may be performed when going to the thermodynamic limit and solving the resultant momentum integral:

$$\begin{aligned} \langle (\phi(x,\tau) - \phi(0,0))^2 \rangle = K \int_0^\infty dk \frac{2}{k} e^{-\alpha k} f_B(uk)(1 - \cos(kx)\cosh(uk\tau)) \\ + K \int_0^\infty dk \frac{1}{k} e^{-\alpha k}(1 - \cos(kx) e^{-uk|\tau|}), \end{aligned} \tag{4.53}$$

where we introduce an ultraviolet cut-off α effectively representing the largest momentum used in the theory. In the limit of zero-temperature only the second integral remains and the expectation value becomes

$$\langle (\phi(x,\tau) - \phi(0,0))^2 \rangle = \frac{K}{2} \log\left(\frac{x^2 + (u|\tau| + \alpha)^2}{\alpha^2} \right). \tag{4.54}$$

When temperature is finite the integral may be solved in the limit where $(x,\tau) \gg \alpha$:

$$\langle (\phi(x,\tau) - \phi(0,0))^2 \rangle = \frac{K}{2} \log\left(\frac{\beta^2 u^2}{\pi^2 \alpha^2} \left[\sinh^2\left(\frac{\pi x}{\beta u}\right) + \sin^2\left(\frac{\pi\tau}{\beta}\right) \right] \right). \tag{4.55}$$

4.3.1 Density-density correlations

To finish treating the density-density correlator we need the expectation value of ϕ derivatives. These can be obtained similarly as to eq. (4.41). The difference enters when Fourier transforming eq. (4.41) in eq. (4.43)

$$\langle \nabla\phi(r_1)\nabla\phi(r_2)\rangle = \frac{1}{(\beta\Omega)^2}\sum_{\mathbf{q}_1,\mathbf{q}_2}(ik_1)\cdot(ik_2)\,\langle\phi(\mathbf{q}_1)\phi(\mathbf{q}_2)\rangle\, e^{i\mathbf{q}_1 r_1+\mathbf{q}_2 r_2}, \quad (4.56)$$

which may be computed as in Sec. 4.3 to yield

$$\langle \nabla\phi(r_1)\nabla\phi(r_2)\rangle = \frac{K}{2\pi^2}\frac{y_\alpha^2-x^2}{\left(x^2+y_\alpha^2\right)^2}, \quad (4.57)$$

where $y_\alpha = u\tau + \alpha\,\mathrm{sgn}(\tau)$ and $x = x_1 - x_2$, $\tau = \tau_1 - \tau_2$. With eq. (4.57) and eq. (4.54) we obtain the density-density correlations from eq. (4.39)

$$\begin{aligned}\langle\rho(x,\tau)\rho(0,0)\rangle = \rho_0^2 &+ \frac{K}{2\pi^2}\frac{y_\alpha^2-x^2}{(x^2+y_\alpha^2)^2}\\ &+A_2\rho_0^2\cos(2\pi\rho_0 x)\left(\frac{\alpha}{r}\right)^{2K}+A_4\rho_0^2\cos(4\pi\rho_0 x)\left(\frac{\alpha}{r}\right)^{8K}+\ldots, \quad (4.58)\end{aligned}$$

where now $r=(x,\tau)$ and A_i are non-universal amplitudes dependent on the specific microscopic model under study.

4.3.2 Green's functions

Notably, the density-density correlations require no discussion of whether the model represents bosonic or fermionic degrees of freedom. When considering Green's functions this distinction becomes important. For bosons we obtain the leading term

$$\langle\psi(r)\psi^\dagger(0)\rangle = \rho_0\,\langle e^{i\theta(r)}e^{-i\theta(0)}\rangle + \ldots. \quad (4.59)$$

Noting that the Hamiltonian eq. (4.35) is symmetric when exchanging

$$\theta\to\phi,\ \phi\to\theta \quad (4.60)$$

$$K\to 1/K,\ u\to u, \quad (4.61)$$

we may repeat the calculations of section. 4.3 made for ϕ using θ instead. Thus the expectation value eq. (4.41) is the same as when using θ with $K\to 1/K$:

$$\langle(\theta(r_1)-\theta(r_2))^2\rangle = \frac{1}{2K}\log\left(\frac{x^2+(u|\tau|+\alpha)^2}{\alpha^2}\right), \quad (4.62)$$

at zero temperature. Similarly, the finite temperature expression follows with $K \to 1/K$. Thus, to lowest order the bosonic Green's function becomes (at zero temperature)

$$\langle \psi(r)\psi^{\dagger}(0)\rangle = A_0\rho_0 \left(\frac{\alpha}{r}\right)^{\frac{1}{2K}} + \ldots. \tag{4.63}$$

This procedure may be performed for fermions as well with the caveat that the lowest-order term is more complex.

5. Self-consistent effective Hamiltonians

5.1 Dimensional crossover and phase transitions in coupled chains

Using a combination of DMRG in an MPS format with MF theory an algorithm, which we name MPS+MF, which computes self-consistently iterated Hamiltonian parameters is developed. The result is an effectively 1D Hamiltonian that describes a 3D system whose higher-dimensional character is contained in the self-consistently determined parameters.

Treatments analogous to MPS+MF have been utilized before for studying e.g. spin systems, such as BPCB [12]. In the present project, the algorithm is used to study an anisotropic Bose-Hubbard model where repulsive interaction occurs only along one direction: the one in which tunneling is strong. The perpendicular directions exhibit weaker tunneling amplitudes giving rise to the anisotropic nature of the model.

The model is studied at commensurate filling where it is possible to study the zero-temperature phase transition driven by repulsion. In addition, the finite temperature transition is studied at the same density. In order to allow comparison to Quantum Monte Carlo (QMC) calculations free from mean-field theory the case of hard-core bosons, i.e. where only one particle is allowed per lattice site is studied. For such systems, where there is no frustration, QMC is free from the sign problem and is the standard method, capable of achieving quasi-exact results with errors decreasing as $1/\sqrt{N}$ with the number of samples, N. In other words, in the considered models QMC is able to produce exact results given enough samples have been collected. Remarkably good agreement between the two methods as to where the zero-temperature quantum phase transition driven by repulsion occurs is found and is identified as a first-order transition between a 3D superfluid to an effectively 1D Mott insulator exhibiting so-called dimensional crossover [28].

Furthermore, critical temperatures for the the finite-temperature second-order transition between a 3D superfluid and the effectively 1D thermal state are computed. However, QMC calculation find critical temperatures at $\sim 70-80\%$ of the value from MPS+MF. Typically, mean-field methods overestimate critical temperatures and the developed MPS+MF method is found to be in better agreement with QMC than with a complete mean-field treatment in which the QMC T_c is only 50% of the full mean-field result [62]. Notably, MPS+MF has different restrictions on its performance than QMC does allowing for promising results where QMC has difficulty performing, e.g., when there is a sign problem.

Additionally, in order to further check the validity of the MPS+MF results a bosonization with mean-field treatment is utilized [29]. The primary difference between this method and MPS+MF is that DMRG is exchanged with TLL theory. In accordance with expectations perfect agreement between analytical and numerical methods in the region where each 1D sub-system behaves like a TLL is found.

Further, the model is studied for no hard-core restrictions allowing several bosons to exist on one site. Similar to the case of hard-core bosons a first-order transition from a 3D superfluid to a 1D Mott insulator occurs when the strength of repulsion is increased. Notably, when bosons exist on the same site the relevant repulsion to be tuned is an on-site interaction as opposed to hard-core bosons. The finite temperature transition from 3D superfluid to thermal state is also found for the case of no hard-core restriction.

In conclusion, great agreement between QMC and MPS+MF is discovered when studying hard-core bosons, which QMC can treat with little issue. In addition, MPS+MF often converges faster and with less resources compared to QMC. Another notable benefit of the developed MPS+MF is that it allows straightforward extension to real-time non-equilibrium dynamics, something which QMC could only manage with great difficulty [63, 64]. It is discovered that systems of this kind exhibit superfluid order at small enough repulsion between bosons and that this order changes discontinuously (in first-order fashion) to insulating order at a critical repulsion value. Notably, the repulsion at which this occurs is larger than the 1D transition from a TLL into a 1D Mott insulator: stronger repulsion is required to enter the insulating state in the self-consistent array of chains.

The developed framework of MPS+MF is further useful since it allows simulation of any 1D system which is weakly coupled to copies of itself. This makes possible the treatment of cases where the 1D sub-systems are described by a massive low-energy theory, i.e. not a TLL, which allows the treatment of cases where bosonization is no longer applicable (or difficult to use).

6. Outlook

The paper included in this licentiate project analyzes bosons using the newly developed MPS+MF algorithm. However, MPS+MF is able to treat any effectively 1D Hamiltonian, even containing several mean-field parameters. Due to the strengths of this approach it is a natural step to attempt similar analyses on fermionic models.

In such models, QMC may begin encountering issues whereas the extension is simple as far as DMRG is concerned. Working with fermionic models is the first step. Initially, studying the reliability of MPS+MF in this context using fermionic models with attraction, which relate to hard-core bosons, will provide a useful testing ground for the method. With attractive interaction the fermionic sign problem should be possible to circumvent and some (e.g. AFQMC [65]) algorithms can provide bases for comparison to MPS+MF.

Continuing, the 1D sub-systems of attractive fermions may be replaced by more complicated models. Since it is known that the quasi-1D repulsive Hubbard ladders exhibit fermionic pairing correlations, stabilizing the large fluctuations in 1D using a reservoir is possible. Letting such a reservoir be played by an infinite array copies of the 1D system, the MPS+MF algorithm should be able to treat even this case. Consequently, making obtainable a model for materials that exhibit superconductivity in which the superconducting pairing correlation's microscopic origin is well understood.

A. Path Integrals

An efficient way to compute observables from a bosonized field theory is the use of path integrals (or functional integral). One reason for this is that Green's functions are time-ordered as a consequence of the method and as such time-ordering does not have to taken into account explicitly.

A.1 Gaussian integration

A path integral over a single complex field with a quadratic action may be written as

$$\int \mathscr{D}\phi e^{-S} = \left(\prod_i \int d\mathrm{Re}[\phi_i] d\mathrm{Im}[\phi_i] \right) e^{-\sum_{i,j} \phi_i^* M_{i,j} \phi_j}. \tag{A.1}$$

The measure $\mathscr{D}\phi$ denotes small variations in the shape of ϕ such that $\int \mathscr{D}\phi$ has the meaning of integration over all possible functions ϕ and is defined by

$$\int \mathscr{D}\phi \equiv \lim_{N\to\infty} \int \prod_{n=1}^{N-1} d\phi_n \tag{A.2}$$

where $d\phi_n$ denote ordinary integration measures representing the variation of ϕ at coordinate slice n. Assuming that M is a complex matrix with positive-definite Hermitian part it is possible to diagonalize it and obtain a set of Gaussian integrals:

$$\int \mathscr{D}\phi e^{-S} = \left(\prod_i \int d\mathrm{Re}[u_i] d\mathrm{Im}[u_i] \right) e^{-\sum_i d_i |u_i|^2} = \frac{\pi^N}{\prod_i d_i} = \pi^N \det M^{-1}, \tag{A.3}$$

where d_i are the matrix elements of M in its diagonal basis. If several fields are included the ϕ_i will be vector-valued and each entry in M is itself a matrix. The previous treatment thus creates one Gaussian set for each field with the same result (M now has twice the linear dimension):

$$\int \mathscr{D}\phi \mathscr{D}\theta e^{-S} = \pi^{2N} \det M^{-1}. \tag{A.4}$$

In order to compute expectation values we need to add source terms h_i and h'_i to the action S

$$\int \mathscr{D}\phi e^{-S_{source}} = \left(\prod_i \int d\mathrm{Re}[\phi_i] d\mathrm{Im}[\phi_i]\right) e^{-\sum_{i,j}\phi_i^* M_{i,j}\phi_j + \sum_i h_i^*\phi_i + \phi_i^* h'_i}, \quad \text{(A.5)}$$

the addition of which can be resolved by completing the square:

$$\int \mathscr{D}\phi e^{-S_{source}} = \pi^N \det M^{-1} e^{\sum_{i,j} h_i^* M_{i,j}^{-1} h'_j}. \quad \text{(A.6)}$$

It is now apparent that path integrals of the form

$$\frac{1}{Z}\int \mathscr{D}\phi (\phi_k^*\phi_l) e^{-S} = \left(\prod_i \int d\mathrm{Re}[\phi_i] d\mathrm{Im}[\phi_i]\right) \phi_k^*\phi_l e^{-\sum_{i,j}\phi_i^* M_{i,j}\phi_j}. \quad \text{(A.7)}$$

may be obtained by applying derivatives of the source term and then setting it to zero e.g.

$$\frac{1}{Z}\int \mathscr{D}\phi (\phi_k^*\phi_l) e^{-S} = \frac{\partial}{\partial h_i}\frac{\partial}{\partial h_j^*}\frac{1}{Z}\int \mathscr{D}\phi e^{-S_{source}}\bigg|_{h,h'=0} = M_{i,j}^{-1}, \quad \text{(A.8)}$$

where

$$Z = \left(\prod_i \int d\mathrm{Re}[\phi_i] d\mathrm{Im}[\phi_i]\right) e^{-\sum_{i,j}\phi_i^* M_{i,j}\phi_j}, \quad \text{(A.9)}$$

is the path integral without added source terms and takes care of the diverging terms of π^N and $\det M^{-1}$. When several fields are included the same strategy may be used where you take care to pick the appropriate component of the matrix $M_{i,j}^{-1}$.

A.2 Bosonization example

Given two (real-valued) conjugate fields ϕ and $\Pi = \frac{1}{\pi}\theta$ such that

$$\left[\phi(x), \Pi(x')\right] = i\delta(x - x') \quad \text{(A.10)}$$

on which the Hamiltonian $H = H[\phi, \Pi] = H[\phi, \theta]$ is dependent we may define the systems partition function with a functional integral

$$\begin{aligned} Z &= \mathrm{Tr}\left[e^{-\beta H}\right] \\ &= \int \mathscr{D}\phi(x,\tau)\mathscr{D}\theta(x,\tau) e^{\int_0^\beta d\tau \int dx \left(i\frac{1}{\pi}\nabla\theta(x,\tau)\partial_\tau\phi(x,\tau) - H[\phi(x,\tau),\theta(x,\tau)]\right)}. \end{aligned} \quad \text{(A.11)}$$

Note that the exponent inside the partition function path integral is the system action

$$S=-\int_0^\beta d\tau\int dx\left(i\frac{1}{\pi}\nabla\theta(x,\tau)\partial_\tau\phi(x,\tau)-H[\phi(x,\tau),\theta(x,\tau)]\right). \tag{A.12}$$

The time ordered correlator of any observables which are functions of the fields ϕ and θ may be obtained from another functional integral

$$\begin{aligned}&\langle T\left[A(x_1,\tau_1)B(x_2,\tau_2)\cdots C(x_N,\tau_N)\right]\rangle\\&=\frac{1}{Z}\int\mathscr{D}\phi(x,\tau)\mathscr{D}\theta(x,\tau)A(\phi(x_1,\tau_1),\theta(x_1,\tau_1))B(\phi(x_2,\tau_2),\theta(x_2,\tau_2))\\&\quad\times\cdots C(\phi(x_N,\tau_N),\theta(x_N,\tau_N))e^{\int_0^\beta d\tau\int dx\left(i\frac{1}{\pi}\theta(x,\tau)\partial_\tau\phi(x,\tau)-H[\phi(x,\tau),\theta(x,\tau)]\right)}.\end{aligned} \tag{A.13}$$

To obtain expectation values we must know how to compute quantities like the ones in eq. (4.48). Assuming the Hamiltonian $H[\phi,\theta]$ is quadratic in the fields. The action can be rewritten in the form (a Fourier transform has been applied to get rid of derivatives)

$$S=-\sum_{q_1,q_2}\Psi^\dagger(q_1)M_{q_1,q_2}\Psi(q_2), \tag{A.14}$$

where

$$\Psi(q)=\begin{pmatrix}\phi_q\\\theta_q\end{pmatrix}. \tag{A.15}$$

Computing the following expectation value:

$$\langle\Psi^*(q_1)\Psi^T(q_2)\rangle=\left\langle\begin{pmatrix}\phi^*_{q_1}\phi_{q_2} & \phi^*_{q_1}\theta_{q_2}\\\theta^*_{q_1}\phi_{q_2} & \theta^*_{q_1}\theta_{q_2}\end{pmatrix}\right\rangle=M^{-1}_{q_1,q_2}, \tag{A.16}$$

thus, it is sufficient to add source terms

$$S_{source}=-\sum_{q_1,q_2}\Psi^\dagger(q_1)M_{q_1,q_2}\Psi(q_2)-\sum_{q_1}h^*_{q_1}\Psi(q_1)+\Psi^\dagger(q_1)h'_{q_1} \tag{A.17}$$

and pick the component of your answer which corresponds to the desired expectation value.

References

[1] H. K. Onnes. The resistance of pure mercury at helium temperatures. *Commun. Phys. Lab. Univ. Leiden*, 1911.

[2] J. Bardeen, L. N. Cooper, and J. R. Schrieffer. Theory of superconductivity. *Phys. Rev.*, 1957.

[3] G. R. Stewart. Unconventional superconductivity. *Adv. Phys.*, 66(2):75–196, apr 2017.

[4] F. Steglich, J. Aarts, C. D. Bredl, W. Lieke, D. Meschede, W. Franz, and H. Schäfer. Superconductivity in the presence of strong Pauli paramagnetism: CeCu2Si2. *Phys. Rev Lett.*, 1979.

[5] D. Jerome, A. Mazaud, M. Ribault, and K. Bechgaard. Superconductivity in a synthetic organic conductor $(TMTSF)_2PF_6$. *J. Phys. Lett.*, 1980.

[6] A. P. Drozdov, M. I. Eremets, I. A. Troyan, V. Ksenofontov, and S. I. Shylin. Conventional superconductivity at 203 kelvin at high pressures in the sulfur hydride system. *Nature*, 525(7567):73–76, 2015.

[7] A. P. Drozdov, P. P. Kong, V. S. Minkov, S. P. Besedin, M. A. Kuzovnikov, S. Mozaffari, L. Balicas, F. F. Balakirev, D. E. Graf, V. B. Prakapenka, E. Greenberg, D A Knyazev, M Tkacz, and M I Eremets. Superconductivity at 250 K in lanthanum hydride under high pressures. *Nature*, 569(7757):528–531, 2019.

[8] E. Dagotto. Correlated electrons in high-temperature superconductors. *Rev. Mod. Phys.*, 1994.

[9] T. A. Maier, M. Jarrell, T. C. Schulthess, P. R.C. Kent, and J. B. White. Systematic study of d-wave superconductivity in the 2D repulsive Hubbard model. *Phys. Rev. Lett.*, 95(23):1–4, 2005.

[10] M. Qin, C. M. Chung, H. Shi, E. Vitali, C. Hubig, U. Schollwöck, S. R. White, and S. Zhang. Absence of Superconductivity in the Pure Two-Dimensional Hubbard Model. *Phys. Rev. X*, 10(3):031016, 2020.

[11] D. J. Scalapino. *Numerical Studies of the 2D Hubbard Model*, pages 495–526. Springer New York, New York, NY, 2007.

[12] M. Klanjšek, H. Mayaffre, C. Berthier, M. Horvatić, B. Chiari, O. Piovesana, P. Bouillot, C. Kollath, E. Orignac, R. Citro, and T. Giamarchi. Controlling Luttinger Liquid Physics in Spin Ladders under a Magnetic Field. *Phys. Rev. Lett.*, 101(13):137207, sep 2008.

[13] T. Giamarchi. Theoretical framework for quasi-one dimensional systems. *Chem. Rev.*, 104(11):5037–56, dec 2004.

[14] T. Nagata, M. Uehara, J. Goto, J. Akimitsu, N. Motoyama, H. Eisaki, S. Uchida, H. Takahashi, T. Nakanishi, and N. Môri. Pressure-Induced Dimensional Crossover and Superconductivity in the Hole-Doped Two-Leg Ladder Compound Sr14-xCaxCu24O41. *Phys. Rev. Lett.*, 81(5):1090–1093, aug 1998.

[15] E. Dagotto. Experiments on ladders reveal a complex interplay between a spin-gapped normal state and superconductivity. *Rep. Prog. Phys.*, 62(11):1525–1571, nov 1999.

[16] C. Bourbonnais and D. Jérome. Interacting Electrons in Quasi-One-Dimensional Organic Superconductors. In A. Lebed, editor, *The Physics of Organic Superconductors and Conductors*, page pp. 358. Springer Berlin Heidelberg, New York, 2007.

[17] R. Blankenbecler, D. J. Scalapino, and R. L. Sugar. Monte Carlo calculations of coupled boson-fermion systems. I. *Phys. Rev. D*, 24(8):2278–2286, 1981.

[18] S. R. White, D. J. Scalapino, R. L. Sugar, E. Y. Loh, J. E. Gubernatis, and R. T. Scalettar. Numerical study of the two-dimensional Hubbard model. *Phys. Rev. B*, 40(1):506–516, jul 1989.

[19] A. Georges, G. Kotliar, W. Krauth, and M. J. Rozenberg. Dynamical mean-field theory of strongly correlated fermion systems and the limit of infinite dimensions. *Rev. Mod. Phys.*, 68(1):13–125, jan 1996.

[20] S. R. White. Density matrix formulation for quantum renormalization groups. *Phys. Rev. Lett.*, 69(19):2863–2866, 1992.

[21] S. R. White. Density-matrix algorithms for quantum renormalization groups. *Phys. Rev. B*, 48(14):10345, 1993.

[22] U. Schollwöck. The density-matrix renormalization group in the age of matrix product states. *Ann. Phys.*, 326(1):96–192, 2011.

[23] T. Giamarchi. *Quantum Physics in One Dimension*. Oxford University Press, New York, 1st edition, 2003.

[24] G. Karakonstantakis, E. Berg, S. R. White, and S. A. Kivelson. Enhanced pairing in the checkerboard Hubbard ladder. *Phys. Rev. B*, 83(5):054508, feb 2011.

[25] T. T. Saraiva, P. J.F. Cavalcanti, A. Vagov, A. S. Vasenko, A. Perali, L. Dell'anna, and A. A. Shanenko. Multiband Material with a Quasi-1D Band as a Robust High-Temperature Superconductor. *Phys. Rev. Lett.*, 125(21):217003, 2020.

[26] V. J. Emery and S. A. Kivelson. Importance of phase fluctuations in superconductors with small superfluid density. *Nature*, 374(6521):434–437, mar 1995.

[27] E. Y. Loh, J. E. Gubernatis, R .T. Scalettar, S. R. White, D. J. Scalapino, and R. L. Sugar. Sign problem in the numerical simulation of many-electron systems. *Phys. Rev. B*, 41(13):9301–9307, 1990.

[28] A. F. Ho, M. A. Cazalilla, and T. Giamarchi. Deconfinement in a 2D optical lattice of coupled 1D Boson systems. *Physical Review Letters*, 92(13):130405, apr 2004.

[29] M. A. Cazalilla, A. F. Ho, and T. Giamarchi. Interacting Bose gases in quasi-one-dimensional optical lattices. *New J. Phys.*, 8(8):158–158, aug 2006.

[30] I. Bloch, J. Dalibard, and S. Nascimbène. Quantum simulations with ultracold quantum gases. *Nat Phys.*, 8(4):267–276, 2012.

[31] T. Fukuhara, A. Kantian, M. Endres, M. Cheneau, P. Schauß, S. Hild, D. Bellem, U. Schollwöck, T. Giamarchi, C. Gross, I. Bloch, and S. Kuhr. Quantum dynamics of a mobile spin impurity. *Nat. Phys.*, 9(4):235–241, 2013.

[32] P. M. Chaikin, T. C. Lubensky, and T. A. Witten. *Principles of condensed matter physics*, volume 10. Cambridge university press, 1st edition, 1995.

[33] J. H. De Boer and E. J.W. Verwey. Semi-conductors with partially and with completely filled 3d-lattice bands. *Proc. Phys. Soc. London*, 49(4S):59–71, aug 1937.

[34] N. F. Mott and R. Peierls. Discussion of the paper by de Boer and Verwey. *Proc. Phys. Soc. London*, 49(4S):72–73, aug 1937.

[35] N. V. Prokof'ev, B. V. Svistunov, and I. S. Tupitsyn. "Worm" algorithm in quantum Monte Carlo simulations. *Phys. Lett. A*, 238(4):253–257, 1998.

[36] M. Boninsegni, N. V. Prokof'ev, and B. V. Svistunov. Worm algorithm and diagrammatic Monte Carlo: A new approach to continuous-space path integral Monte Carlo simulations. *Phys. Rev. E*, 74(3):36701, sep 2006.

[37] O. F. Syljuåsen and A. W. Sandvik. Quantum Monte Carlo with directed loops. *Phys. Rev. E*, 66(4):46701, 2002.

[38] I. P. McCulloch. Infinite size density matrix renormalization group, revisited. apr 2008.

[39] G. Vidal. Classical Simulation of Infinite-Size Quantum Lattice Systems in One Spatial Dimension. *Phys. Rev. Lett.*, 98(7):70201, feb 2007.

[40] T. Köhler, J. Stolpp, and S. Paeckel. Efficient and Flexible Approach to Simulate Low-Dimensional Quantum Lattice Models with Large Local Hilbert Spaces, 2020.

[41] N. Chepiga and S. R. White. Comb tensor networks. *Phys. Rev. B*, 99(23):235426, jun 2019.

[42] Kenneth G Wilson. The renormalization group: Critical phenomena and the Kondo problem. *Rev. Mod. Phys.*, 47(4):773–840, 1975.

[43] U. Schollwöck. The density-matrix renormalization group. *Rev. Mod. Phys.*, 77(1):259–315, apr 2005.

[44] I. P. McCulloch. From density-matrix renormalization group to matrix product states. *J. Stat. Mech: Theory Exp.*, 2007(10):P10014—-P10014, 2007.

[45] G. Vidal. Efficient Classical Simulation of Slightly Entangled Quantum Computations. *Phys. Rev. Lett.*, 91(14):147902, oct 2003.

[46] G. Vidal. Efficient Simulation of One-Dimensional Quantum Many-Body Systems. *Phys. Rev. Lett.*, 93(4):040502, jul 2004.

[47] J. Dukelsky, M. A. Martín-Delgado, T. Nishino, and G. Sierra. Equivalence of the variational matrix product method and the density matrix renormalization group applied to spin chains. *Europhys. Lett.*, 43(4):457–462, aug 1998.

[48] I P McCulloch and M Gulácsi. Comment on "Equivalence of the variational matrix product method and the density matrix renormalization group applied to spin chains" by J. Dukelsky et al. *Europhys. Lett.*, 61(1):138–139, jan 2003.

[49] J. Dukelsky, M. A. Martín-Delgado, T. Nishino, T. Wada, and G. Sierra. Reply to the Comment by P. McCulloch and M. Gulácsi on"Equivalence of the variational matrix product method and the density matrix renormalization group applied to spin chains". *Europhys. Lett.*, 61(1):140–141, jan 2003.

[50] F. Verstraete, J. J. García-Ripoll, and J. I. Cirac. Matrix Product Density Operators: Simulation of Finite-Temperature and Dissipative Systems. *Phys. Rev. Lett.*, 93(20):207204, nov 2004.

[51] S. R. White and D. A. Huse. Numerical renormalization-group study of low-lying eigenstates of the antiferromagnetic S=1 Heisenberg chain. *Phys. Rev. B*, 48(6):3844–3852, aug 1993.

[52] Ö. Legeza and G. Fáth. Accuracy of the density-matrix renormalization-group method. *Phys. Rev. B*, 53(21):14349–14358, jun 1996.

[53] F. Bloch. Bremsvermögen von Atomen mit mehreren Elektronen. *Z. Angew. Phys.*, 81(5):363–376, 1933.

[54] E. Fradkin. *Field theories of condensed matter physics*. 2nd edition, 2013.

[55] S. I. Tomonaga. Remarks on Bloch's Method of Sound Waves applied to Many-Fermion Problems. *Prog. Theor. Phys.*, 5(4):544–569, jul 1950.

[56] A. Luther and I. Peschel. Calculation of critical exponents in two dimensions from quantum field theory in one dimension. *Phys. Rev. B*, 12(9):3908–3917, nov 1975.

[57] S. Mandelstam. Soliton operators for the quantized sine-Gordon equation. *Phys. Rev. D*, 11(10):3026–3030, 1975.

[58] E. Witten. Nonabelian bosonization in two dimensions. *Comm. Math. Phys.*, 92(4):455–472, 1984.

[59] A. O. Gogolin, A. A. Nersesyan, and A. M. Tsvelik. *Bosonization and strongly correlated systems*. Cambridge university press, 2004.

[60] G. D. Mahan. *Many-particle physics*. Springer, 3rd edition, 2000.

[61] A. L. Fetter and J. D. Walecka. *Quantum Theory of Many-particle Systems*. Dover Books on Physics. Dover Publications, 1st edition, 2003.

[62] J. Carrasquilla and M. Rigol. Superfluid to normal phase transition in strongly correlated bosons in two and three dimensions. *Phys. Rev. A*, 86(4):043629, oct 2012.

[63] L. Mühlbacher and E. Rabani. Real-Time Path Integral Approach to Nonequilibrium Many-Body Quantum Systems. *Phys. Rev. Lett.*, 100(17):176403, 2008.

[64] P. Werner, T. Oka, and A. J. Millis. Diagrammatic Monte Carlo simulation of nonequilibrium systems. *Phys. Rev. B*, 79(3):35320, jan 2009.

[65] M. Motta and S. Zhang. Ab initio computations of molecular systems by the auxiliary-field quantum Monte Carlo method. *WIREs Comput. Mol. Sci.*, 8(5):e1364, 2018.

Paper I

PHYSICAL REVIEW B **102**, 195145 (2020)

Dimensional crossover and phase transitions in coupled chains: Density matrix renormalization group results

Gunnar Bollmark,[1] Nicolas Laflorencie,[2] and Adrian Kantian[1]

[1]*Department of Physics and Astronomy, Uppsala University, Box 516, S-751 20, Uppsala, Sweden*

[2]*Laboratoire de Physique Théorique, CNRS and Université de Toulouse, 31062 Toulouse, France*

(Received 6 May 2020; revised 3 November 2020; accepted 4 November 2020; published 24 November 2020)

Quasi-one-dimensional (Q1D) systems, i.e., three- and two-dimensional (3D/2D) arrays composed of weakly coupled one-dimensional lattices of interacting quantum particles, exhibit rich and fascinating physics. They are studied across various areas of condensed matter and ultracold atomic lattice-gas physics, and are often marked by dimensional crossover as the coupling between one-dimensional systems is increased or temperature decreased, i.e., the Q1D system goes from appearing largely 1D to largely 3D. Phase transitions occurring along the crossover can strongly enhance this effect. Understanding these crossovers and associated phase transitions can be challenging due to the very different elementary excitations of 1D systems compared to higher-dimensional ones. In the present work, we combine numerical matrix product state (MPS) methods with mean-field (MF) theory to study paradigmatic cases of dimensional crossovers and the associated phase transitions in systems of both hard-core and soft-core lattice bosons, with relevance to both condensed matter physics and ultracold atomic gases. We show that the superfluid-to-insulator transition is a first order one, as opposed to the isotropic cases, and calculate transition temperatures for the superfluid states, finding excellent agreement with analytical theory. At the same time, our MPS + MF approach keeps functioning well where the current analytical framework cannot be applied. We further confirm the qualitative and quantitative reliability of our approach by comparison to exact quantum Monte Carlo calculations for the full 3D arrays.

DOI: 10.1103/PhysRevB.102.195145

I. INTRODUCTION

Quasi-one-dimensional (Q1D) systems, 3D arrays of weakly coupled 1D quantum systems, appear in a wide variety of solid state materials and can readily be realized in lattice-confined ultracold atomic gases. On the materials side, there is very active research into weakly coupled spin chains and ladders such as BPCB [1,2] and related magnetic compounds [3–5], the organic Bechgaard and Fabre salts (“the organics”) [6–10], the strontium-based telephone number compounds [11,12], and chromium pnictide [13,14], all three of which are itinerant systems which can be made to enter an unconventionally superconducting (USC) state. Of these, the organics, preceding the high-T_c cuprate superconductors as the first USC materials [15], have received the most in-depth research. Much of this is due to the abiding challenge of resolving the microscopic origin of repulsion-mediated electron pairing as well as the direct transition between the USC state based on this pairing and an insulating magnetically ordered one, analogous to that found in the cuprates, which is of first-order type in the organics [9]. The fascination of the organics is further enhanced by their exhibition of *dimensional crossover* (DC), shown by various quantum spin systems as well [3,16–18], where the systems effective dimensionality increases from 1D to 2D and eventually 3D, as quantum coherence between the constituent 1D systems increases with decreasing temperature and/or increased (but still weak) intersystem coupling. These DCs can further be marked by a phase transition occurring along the crossover, where DC can then be particularly sharp; for example, the opening of a gap in each constituent 1D system can make it much harder for intersystem coupling to establish coherence and thus ordering in the transverse direction will be much weaker.

The concept of DC taking place around a phase transition is especially interesting for the theory of the USC state, as it is in Q1D models alone that the transition into a superconducting state based on repulsively mediated pairing of fermions can be understood at the fundamental level, at least qualitatively. The prime models for this are 3D arrays of doped, weakly coupled Hubbard ladders. Here, fusing Tomonaga-Luttinger-liquid (TLL) theory for the single ladder [19] with either static mean-field (MF) theory [20] or alternatively renormalization group treatments [7] allows a qualitative description of the transition to the USC state as the system crosses over from effectively uncoupled 1D Hubbard ladders to the 3D ordered array as temperature decreases.

Going from such a fundamental, qualitative description of the phase transition marking this specific DC to one allowing for quantitative accuracy has stayed an open challenge for which the theoretical tools remain to be developed. Under-

---

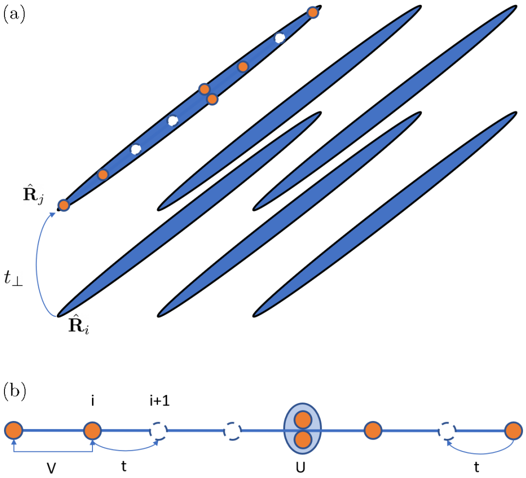

FIG. 1. A schematic representation of the model described by Eq. (1) where (a) represents the 3D model and (b) the 1D subsets of the full 3D model.

standing DC and their associated transitions in general with quantitative and even qualitative theory can be very difficult, such as in the case of the organics, because the basis of collective density excitations used to describe the 1D system are completely different from the one of Landau or Bogoliubov quasiparticles used for 2D and 3D systems.

The present work is thus motivated by the twin challenge of developing better theory for DC and associated phase transitions in Q1D-systems in general, as well as specifically for the case of the transition into the USC phase in the Hubbard-ladder array. As a first step towards this end we set up a comparatively simple model, 3D arrays formed from weakly coupled chains of interacting lattice bosons with short-range interactions (cf., Fig. 1). As will be shown and discussed, this class of models combines several advantages: (i) They show multiple interesting DCs and associated phase transitions, including first-order transitions (like the organics do between the USC and a magnetically ordered insulating phase) and possibly mixed-order transitions. (ii) They are perfect testbeds to further advance efficient yet remarkably accurate numerics based on combinations of matrix product states (MPS) and MF pioneered, e.g., in Ref. [1]. Crucially, the accuracy of these MPS + MF numerics can be ascertained by the gold standard for 2D/3D lattice bosons, quantum Monte Carlo (QMC) simulations. (iii) Our MPS + MF numerics can be checked directly against fit-free TLL + MF analytical theory used for the thermal transition to the superfluid regime [21,22]. Additionally, our numerics will work in regimes where TLL + MF is no longer applicable as well as making possible efficient real-time many-body dynamics for Q1D systems. (iv) When specializing the study model to the case of hard-core bosons (HCBs) with nearest-neighbor (n.n.) repulsion, it admits mapping to Q1D arrays of doped Hubbard ladders at the level of low-energy, long-wavelength effective TLL theory. (v) These systems either already admit realization in many existing experiments on ultracold lattice gases, including the possibility of observing mixed-order DC, or, in the case of HCBs with n.n. repulsion, may do so within the foreseeable future [23,24].

The present paper is thus structured as follows: Section II describes the Q1D array model of bosonic chains and introduces the transverse MF approximation. Section III describes the MPS + MF method we use for fast, efficient calculations of the systems properties for ground and thermal states. Details of the QMC calculations are also given. Section IV discusses the zero-temperature first-order transition we find between a 3D superfluid (SF) and a 1D charge-ordered (CO) phase for HCBs with increasing n.n. repulsion and the similar transition observed for soft-core bosons at integer filling. We also study the transition between SF and a thermal gas with rising temperature. The results of the MPS + MF approach are compared against both QMC and TLL + MF analytics and found to range from excellent to highly satisfactory. In Sec. V we summarize the validity of the MPS + MF approach to phase transitions in bosonic systems and discuss the implications of our results for DC physics in other systems as well as consider the efficiency of MPS + MF in comparison with QMC. Section VI then provides an outlook on future research on the basis of the present work.

II. MODEL

In this work, we consider extended Bose-Hubbard models with anisotropic tunneling strength. We first focus on hard-core bosons (HCB), for which the number of allowed particles is restricted to one boson per site. Further, to connect with established experiments we can also lift this restriction of one boson per site and consider the more general case of soft-core bosons (SCB).

A. Three-dimensional Hamiltonian

The full Hamiltonian is given by the expression

$$\begin{aligned} H_B = & -t \sum_{\{\hat{\mathbf{R}}_i\}} b^\dagger_{\hat{\mathbf{R}}_i+\hat{\mathbf{x}}} b_{\hat{\mathbf{R}}_i} + \text{H.c.} - \mu \sum_{\{\hat{\mathbf{R}}_i\}} b^\dagger_{\hat{\mathbf{R}}_i} b_{\hat{\mathbf{R}}_i} \\ & + \frac{U}{2} \sum_{\{\hat{\mathbf{R}}_i\}} n_{\hat{\mathbf{R}}_i} \left(n_{\hat{\mathbf{R}}_i} - 1 \right) + V \sum_{\{\hat{\mathbf{R}}_i\}} n_{\hat{\mathbf{R}}_i+\hat{\mathbf{x}}} n_{\hat{\mathbf{R}}_i} \\ & - t_\perp \sum_{\{\hat{\mathbf{R}}_i\}, \hat{\mathbf{a}} \in [\hat{\mathbf{y}}, \hat{\mathbf{z}}]} b^\dagger_{\hat{\mathbf{R}}_i+\hat{\mathbf{a}}} b_{\hat{\mathbf{R}}_i} + \text{H.c.} \\ = & \, H_t + H_\mu + H_U + H_V + H_{t_\perp}, \end{aligned} \tag{1}$$

where $\{\hat{\mathbf{R}}_i\}$ denotes the set of all lattice points, ${b^\dagger}_{\hat{\mathbf{R}}_i}$ ($b_{\hat{\mathbf{R}}_i}$) is the creation (annihilation) operator associated with the site at $\hat{\mathbf{R}}_i$, and $n_{\hat{\mathbf{R}}_i} = {b^\dagger}_{\hat{\mathbf{R}}_i} b_{\hat{\mathbf{R}}_i}$ is the number operator on that site. We have set the lattice spacing $a = 1$.

The transverse hopping $t_\perp$ governs two directions and the longitudinal hopping one direction. In this paper we consider cases where $t_\perp/t \ll 1$. Further, we restrict ourselves to $U, V > 0$, i.e., repulsive interactions. In addition, note that the repulsive interaction V between nearest neighbors only occurs along the strong tunneling direction.

B. Local Hilbert space truncation

The Hamiltonian Eq. (1) allows any number of bosons on one site: $\langle n_i \rangle \in [0, \infty]$. In the hard-core case, $U \to \infty$, such that $0 \leqslant \langle n_i \rangle \leqslant 1$. In the soft-core case we let $0 \leqslant \langle n_i \rangle \leqslant 3$. This cutoff of three bosons per site is chosen such that projections onto states of larger occupation number carry a small weight:

$$\langle \Psi | P_4(i) | \Psi \rangle \leqslant 10^{-4}, \tag{2}$$

where $P_4(i)$ is the projector onto the state of four bosons on site i. For SCB the value of U is of course very important and will be specified, while for simplicity we fix $V = 0$ in this model.

C. Quasi-1D Hamiltonian

We wish to use the density matrix renormalization group (DMRG) algorithm in matrix product state (MPS) formalism [25,26] to solve our problem. However, calculations on 3D models using DMRG scale very poorly with system size. To bypass this issue we reduce the problem to solving an effectively one-dimensional (1D) model using mean-field theory. We consider fluctuations around an order parameter

$$b_{\hat{\mathbf{R}}_i} = \langle b_{\hat{\mathbf{R}}_i} \rangle + \delta b_{\hat{\mathbf{R}}_i} \tag{3}$$

and ignore terms in the Hamiltonian of order $\mathcal{O}(\delta b^2)$. We make this substitution only in the transverse hopping Hamiltonian $H_{t_\perp}$. If we consider open boundary conditions (OBC) this yields the Q1D Hamiltonian

$$\begin{aligned} H_{\mathrm{SMF}}(\alpha) = {} & -t \sum_{i+1}^{L-1} b_{i+1}^\dagger b_i + \mathrm{H.c.} - \mu \sum_{i=1}^{L} b_i^\dagger b_i \\ & + \frac{U}{2} \sum_{i=1}^{L} n_i(n_i - 1) \\ & + V \sum_{i=1}^{L-1} n_{i+1} n_i - \alpha \sum_{i=1}^{L} (b_i^\dagger + b_i), \end{aligned} \tag{4}$$

where indices i have been introduced which indexes the site of a one-dimensional subset of the 3D model in the longitudinal direction. In this work we will use both OBC and periodic boundary conditions (PBC), the latter in which we have the additional condition of $b_{L+1} = b_1$ and the term

$$H_L = -t(b_1^\dagger b_L + \mathrm{H.c.}) + V n_1 n_L \tag{5}$$

must be added to the Hamiltonian Eq. (4).

We only decouple the 3D system transversely since the coupling $t_\perp / t \ll 1$ is small by choice. We have routinely ignored any constant contribution to the Hamiltonian. The new coupling α is obtained as

$$\alpha^{(*)} = z_c t_\perp \langle b^{(\dagger)} \rangle, \tag{6}$$

where $z_c = 4$ is the coordination number for a simple cubic lattice and we have assumed that α is real. We will call the constant α a boson injection/ejection amplitude. Notably, the only difference between a 2D and 3D anisotropic system in this approach is z_c. A schematic representation of this model is shown in Fig. 1.

III. METHODS

To find ground states and thermal states of the Hamiltonian Eq. (1) two methods will be used. The first one is comprised of using DMRG to solve the Q1D Hamiltonian Eq. (4). We then use quantum Monte Carlo (QMC) simulations [27] for the simplest case of hard-core bosons that we can directly compare with DMRG results.

A. DMRG with static mean-field

Since Eq. (4) is a one-dimensional Hamiltonian, the DMRG algorithm scales well with system size and can be used to compute ground states and thermal states [26]. The additional cost to this method is the self-consistent determination of α. We will call the outlined procedure MPS + MF for the remainder of this paper.

1. Boson injection convergence

The self-consistent routine starts with guessing a boson injection amplitude α_0 and then computing a new value α_1

$$\alpha_1 = z_c t_\perp \langle b \rangle_0, \tag{7}$$

where $\langle \, \rangle_0$ denotes an average with Hamiltonian $H_{\mathrm{SMF}}(\alpha_0)$ defined by Eq. (4) with $\alpha = \alpha_0$ and b is in principle any b_i given an infinite system though in practice an average over several sites. Extending the relation to an arbitrary number of loops simply yields

$$\alpha_{n+1} = z_c t_\perp \langle b \rangle_n. \tag{8}$$

Several exit conditions of the self-consistent loop can be used. Different observables converge at various rates (e.g., density typically converges quickly). In the present case, we use the Bose-Einstein condensate (BEC) order parameter as the observable for determining whether the self-consistent calculation has converged with the condition

$$\left| \frac{\langle b \rangle_n - \langle b \rangle_{n-1}}{\langle b \rangle_{n-1}} \right| < \epsilon_{\langle b \rangle}. \tag{9}$$

The quantity $\epsilon_{\langle b \rangle} = 10^{-4}$ is an error tolerance which can be selected to desired convergence error.

The convergence error should be the largest error in the problem. Any other larger error scale allows α to fluctuate within that scale which disallows settling on a value to convergence precision. An example of such a potential error scale is the truncation error inherent to DMRG.

The fast convergence of this algorithm is highly dependent on how good the initial guess is. Therefore, we have found it good practice to implement some guessing heuristic. For the data shown in this paper, we select an initial value of α which places us above the converged value and check the trend of the computed values of α. For the models we consider this trend is usually exponential. Restarting the whole algorithm using the extrapolated value from an exponential fit as initial guess typically brings you closer to the correct value. Thereby the number of loops required for convergence is reduced.

When using this approach we ran into slow-downs of the self-consistent loop convergence close to phase transitions. If no extrapolation scheme as described previously is used, convergence at transition points may require intractably many loops.

2. Density targeting

One issue in the mean-field treatment presented in Eq. (4) is that the Hamiltonian is transformed from representing a particle number-conserving system to one of nonconservation. Physically, this means that while the particle number is conserved in the full 3D system each individual chain may exchange particles with other chains thus upsetting the conserved particle number locally.

Often we wish to fix the density of an individual chain to some value n_0 and must choose the corresponding chemical potential μ. When converging α in the self-consistent loop, the density for one value of α may have different dependence on μ than for other α s.t.

$$n_{\alpha_n}(\mu) \neq n_{\alpha_{n+1}}(\mu), \tag{10}$$

where

$$n_{\alpha_n} = \frac{1}{L}\sum_{i=1}^{L} \langle n_i \rangle_{\alpha_n}. \tag{11}$$

This means that in addition to converging α self-consistently we must do the same for μ simultaneously. This procedure involves the measurement of density each loop and then the calculation of a new chemical potential that gives you the desired density.

Due to this issue the cost of computation increases as each new μ requires a new state calculation to verify the density, i.e., one self-consistent loop may require several DMRG computations. Fortunately, the density typically converges faster than α and the performance is not greatly affected by the fixation of μ in the cases considered in this paper. The density is compared to a chosen target and must fulfill the following condition

$$\frac{|n_{\alpha_n} - n_{\text{target}}|}{n_{\alpha_n}} < \epsilon_n, \tag{12}$$

where $\epsilon_n = 10^{-5}$ is the error tolerance used for densities in calculations.

B. DMRG observables

When using DMRG we will consider two observables to characterize the studied phases. The BEC order is evaluated by measuring the expectation values $\langle b_i \rangle$. When these are finite it means that there is a finite probability for particles to tunnel in and out of the quasi-1D system described by Eq. (4), i.e., the boson injection/ejection amplitude is nonzero. This quantity is our mean-field order parameter and it is computed by averaging over several sites of the quasi-1D model

$$\langle b \rangle = \frac{1}{i_l - i_f + 1}\sum_{i=i_f}^{i_l} \langle b_i \rangle, \tag{13}$$

where i_f (i_l) is the first (last) site to be included in the average. This calculation assumes that there is no preferential site in the quasi-1D system from which to tunnel in or out. The choice of $i_f,\ i_l$ depends on the boundary conditions. This means that OBC requires an average of the systems central sites to avoid boundary effects while PBC is free from this issue as all sites are equivalent.

Typically, DMRG is more efficient with OBC. However, in the hard-core case, OBC gives the system large boundary effects, as is shown in Appendix A. Thus, the boundary conditions we will use when resolving the SF-CDW transition are PBC for the hard-core case and OBC for the soft-core case.

To characterize CDW phases we compute the charge gap, i.e., the energy required to add or remove one particle from the system. Since the Hamiltonian Eq. (4) does not conserve particle number we will, in this work, define the charge gap as the width in μ of density plateaus

$$\Delta_\rho = \mu_{\text{upper}} - \mu_{\text{lower}}, \tag{14}$$

where the chemical potentials at the plateau edges are defined by

$$n(\mu) = \text{const.}, \mu \in [\mu_{\text{lower}}, \mu_{\text{upper}}] \tag{15}$$

$$n(\mu_{\text{upper}} + \delta) > n(\mu_{\text{upper}}) \tag{16}$$

$$n(\mu_{\text{lower}} - \delta) < n(\mu_{\text{lower}}), \tag{17}$$

where $\delta > 0$ is a small addition (subtraction) of the chemical potential. Further details about the charge gap are given in Appendix B.

1. Truncation error extrapolation of DMRG observables

In order for results from a DMRG solution to be reliable an extrapolation to zero truncation error is required [26]. This is done for all observables X using a linear fit to the data points [28]:

$$X = X_0 + c_0\epsilon_t. \tag{18}$$

We find for OBC that this expression fits not only energies but also measurements of the order parameter Eq. (13).

Using OBC the truncation error is small even for a modest bond dimension as low as $\chi = 50$. Extrapolations to zero truncation error yield no improvements within the self-consistent error. On such occasion we do not perform extrapolations and use the largest bond dimension (smallest truncation error) available.

We note that when using PBC quite large bond dimensions are required. When computing charge gaps we have found truncation errors as large as $\epsilon_t \sim 10^{-5}$ for a bond dimension of $\chi = 250$. Further, the manner in which charge gaps are computed in this paper carries an additional error (see Appendix B). This has made extrapolations in truncation error difficult. As a result, the charge gap data in Fig. 2(a) comes with the caveat that it is affected by notable truncation errors.

2. Finite size extrapolation of DMRG observables

The type of DMRG used in the MPS + MF method is finite size DMRG to make onsite measurements and correlator measurements possible. We are often interested in the thermodynamic behavior of a system and thus we must extrapolate results to the limit of infinitely large systems. The extrapolation scheme used depends on the observable that is being measured.

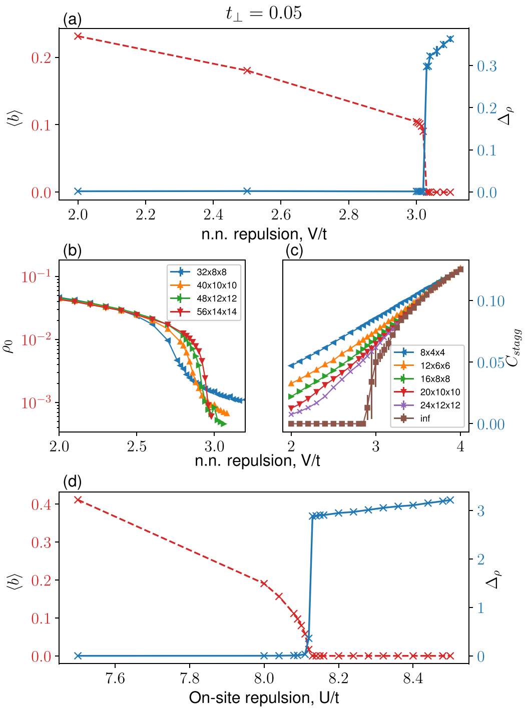

FIG. 2. A comparison of the order parameters characterizing the two ordered phases at $T = 0$ at $t_\perp/t = 0.05$. The red dashed line is the BEC order parameter and the blue solid line the charge gap (which can be seen as the charge density wave order parameter). (a) MPS + MF results for a hard-core constraint model with filling fraction $n = 0.5$ using PBC. (b) QMC for hard-core boson model with BEC order parameter Eq. (23) size dependence. (c) QMC for hard-core boson model with the CDW order parameter Eq. (22) size dependence. (d) MPS + MF results for a soft-core boson model with filling fraction $n = 1.0$ using OBC.

For the charge gap we use a second degree polynomial fit in L^{-1}:

$$\Delta_\rho(L) = c_0 + c_1\frac{1}{L} + c_2\frac{1}{L^2} + \mathcal{O}\left(\frac{1}{L^3}\right). \tag{19}$$

This expression is commonly used to fit the finite size dependence of energies. We find that our charge gap measurements fit this ansatz as well.

For the order parameter we use two different fitting forms. When used to characterize the finite-temperature second-order normal to superfluid phase transition we use a power-law expression

$$\langle b \rangle(L) = c_0 + c_1 L^{-c_2}. \tag{20}$$

This expression is known to hold analytically at the transition point, and we find our data for finite temperature fits Eq. (20) quite well.

For the first order zero-temperature transitions from superfluid to CDW we use a second order polynomial for the squared order parameter

$$\langle b \rangle^2 = c_0 + c_1\frac{1}{L} + c_2\frac{1}{L^2} + \mathcal{O}\left(\frac{1}{L^3}\right). \tag{21}$$

These expressions hold close to phase transitions which is also the area where finite size effects are most prominent. Concrete examples of such extrapolations are provided in Appendix E.

Frequently, the largest error of the MPS + MF approach is from the self-consistent convergence as opposed to finite size errors. When this occurs, fitting to one of the forms Eqs. (19)–(21) is difficult and yields poor fits. On these occasions we find that larger sizes do not change measured value outside of the self-consistent error and we use the largest size measurement available.

C. Quantum Monte Carlo

Our large-scale QMC simulations have been performed with the stochastic series expansion (SSE) algorithm [27] on 3D arrays of coupled chains, using anisotropic lattices of sizes $L_x \times L_y \times L_z$, with $L_x = L$ and $L_y = L_z = L/f$ for an integer f. We have only focused on the case of HCB, but extending to SCF is straightforward. Note also that PBC are used in all directions.

In order to address the bosonic phases and associated transitions for the 3D model Eq. (1) at both zero and finite temperatures, we compute the three following observables. Charge density wave order is evaluated with the staggered correlation function at mid-distance, along the chain directions

$$C_{\text{stagg.}} = \frac{1}{N}\sum_i (-1)^{L/2}(\langle n_i n_{i+L/2}\rangle - \langle n_i\rangle\langle n_{i+L/2}\rangle), \tag{22}$$

where the sum is performed over the $N = L^3/8$ sites and where $f = 2$ has been used for the aspect ratio. The BEC order parameter (condensate density) is obtained by summing off-diagonal correlators

$$\rho_0 = \frac{1}{N^2}\sum_{i,j}\langle b_i^\dagger b_j\rangle, \tag{23}$$

where an aspect ratio of $f = 4$ has been used.

The superfluid response can be evaluated for longitudinal (intrachain) and transverse (interchain) directions with the superfluid stiffness

$$\rho_{S,\parallel(\perp)} = \frac{1}{N}\frac{\partial^2 E_0(\varphi_{\parallel(\perp)})}{\partial\varphi^2_{\parallel(\perp)}}\bigg|_{\varphi_{\parallel(\perp)}=0}. \tag{24}$$

In the above definition, E_0 is the total energy, and $\varphi_{\parallel(\perp)}$ is a small twist angle enforced on all bonds in both longitudinal and transverse directions. Technically, the superfluid stiffness [29] is efficiently measured via the fluctuations of the winding number [30] during the SSE simulation [31].

IV. RESULTS

For most of the results we perform three different types of calculations: (i) an MPS + MF calculation of both ground and thermal states for hard-core bosons which we also compare with (ii) a correspondent QMC calculation and finally (iii) calculations of both ground and thermal states for soft-core bosons using MPS + MF. For MPS + MF, a bond dimension of $\chi = 50$ has been used with OBC. For PBC we instead use a bond dimension of $\chi = 250$. As stated in Sec. III B 1 truncation error extrapolation has proved difficult since other error sources are dominant. Nevertheless, such extrapolations have been used where possible. We have omitted error bars where the error is smaller than the symbol size in all figures. For all data, the error due to truncation error is much smaller than other sources and we omit such analyses.

First, we analyze the system when interaction strength U, V is varied. We choose to analyze commensurate densities, where we expect quantum phase transitions to occur at zero temperature. In the hard-core case it is known that charge ordering occurs for a half-filled isolated chain via a Berezinskii-Kosterlitz-Thouless (BKT) transition at $V_c = 2t$ [32]. This particular density $n = \frac{1}{L}\sum_{i=1}^{L}\langle n_i\rangle = 0.5$ is interesting as it forces the system to incur some energy penalty along with an energy gain from hopping due to the repulsive interaction. We expect there to be a charge-ordering transition for the quasi-1D model as well but with a shifted V_c compared to the 1D case.

For the soft-core case we instead target $n = 1$ and fix $V = 0$ to simplify the analysis. This unit-filled regime with only local repulsions can generally be expected to yield some type of order-to-order phase transition [33].

Second, we analyze the same systems but at finite temperature. We are primarily interested in the critical temperature and how it depends on the microscopic parameters of the Hamiltonian. In this context, we are interested in how accurate our approximate (but numerically low-cost) MPS + MF-based calculations of T_c are in comparison to those from quasiexact QMC.

A. Zero temperature results

For small values of repulsion we expect there to be a BEC superfluid (SF) phase. At large values of repulsion, the system should become insulating and exhibit a charge-ordered phase (CDW). To analyze this transition we fix $t_\perp/t = 0.05$.

1. BEC/superfluid to CDW at T = 0

MPS + MF results are shown in Fig. 2(a) where the charge gap is plotted together with the BEC order parameter as a function of the nearest-neighbor repulsion V. Note that for an isolated 1D system the transition into CDW occurs at $V/t = 2$ whereas in the quasi-1D case we discuss here, the transition is pushed to quite a higher value $V_c/t \approx 3.02$, while $t_\perp/t = 1/20$ is small. Importantly, one observes clear discontinuities for both order parameters at V_c, indicating a first-order transition between a gapless BEC-SF and a CDW insulator. The MPS + MF results can be directly compared to the QMC simulations shown in Figs. 2(b) and 2(c). The agreement is very good, since QMC results find a first-order transition for $V_c/t \approx 3$, the first-order (discontinuous step) character of the transition becoming more and more evident upon increasing system size.

QMC data in Figs. 2(b) and 2(c) show strong finite size effects, which are more pronounced close to the transition. The BEC density ρ_0 [panel (b)] is shown for an aspect ratio of 4. There, $\rho_0(L)$ becomes steeper when increasing system size, a trend which is clearly compatible with a small but finite jump at the thermodynamic limit. This is further discussed in Appendix C where such a jump is more visible due to a larger value of the transverse tunneling. The CDW order parameter C_{stagg}, shown in Fig. 2(c), has been computed for a different aspect ratio of 2 in order to get a better convergence towards the thermodynamic limit. Using a general finite size scaling of the form

$$C_{\text{stagg}}(L) = C_{\text{stagg}}^{\infty} + A/L^{B}\exp(-L/\xi), \qquad (25)$$

a very good description of finite size data is obtained. The infinite size extrapolation $C_{\text{stagg}}^{\infty}$, plotted against V/t, is clearly compatible with a jump at the transition. Note however the strong error bars in the critical regime, characteristic of a first order transition.

The soft-core boson data has been computed for $V = 0$. Since we fix the density to $n = 1.0$ a nearest neighbor repulsion would disturb the potential Mott insulator that can be established at large U. In Fig. 2(c) a transition to the CDW phase can be seen at $U_c/t \approx 8.12$. This strongly contrasts with the isolated chain case where a BKT transition occurs for a much smaller onsite repulsion at $U_c/t \approx 3.3$ [34].

At the transition point the charge gap attains a large value seemingly discontinuously while no such strong first order behavior is apparent when considering the order parameter. It is possible that the latter has a jump so small that it is undetectable by the current method we are using (see Sec. V).

B. Finite temperature

Using the MPS + MF method it is also possible to obtain thermal averages [26], while for QMC finite temperature is natural. Thus, we next investigate $T > 0$ physics.

1. SF to normal

An interesting transition that should occur for finite temperature is that of 3D superfluid to a thermal gas (the normal or disordered phase). We wish to compute the critical temperature where the system looses BEC coherence and enters the normal phase. We will let the repulsion vary in the system to see how critical temperature is affected. Since we are mainly interested in the SF to normal phase transition we will stay away from values of the repulsion in which there is no SF even at zero temperature, i.e., we stay at $V/t < 3$ for hard-core bosons and $U/t < 8.12$ for soft-core bosons.

The critical temperature of the transition can be found by finding the point at which $\langle b\rangle \to 0$ in the thermodynamic limit. From Fig. 3 it is clear that for $t_\perp/t = 0.05$ this point lies close to $T/t = 0.4$. An important question using our MPS + MF approach is how accurate the observed critical temperatures are (i.e., how incorrect is the mean-field approximation). A full mean field analysis overestimates the critical temperatures by a factor of 2 compared to exact calculations using QMC in the 3D case [35]. Hence, it is important to determine if and by how much our MPS + MF hybrid approach improves upon this factor.

We have therefore performed finite-T QMC simulations of the full 3D Hamiltonian Eq. (1). We determine the critical temperatures using standard finite-size scaling analysis which

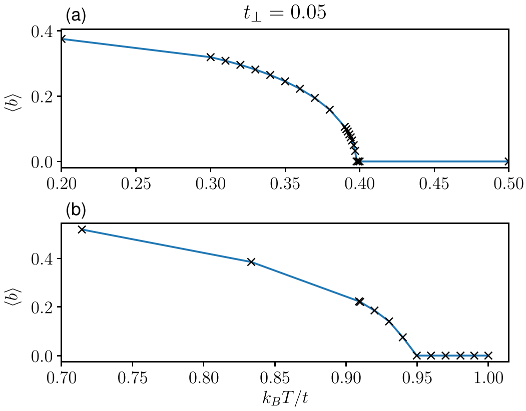

FIG. 3. A plot of the superfluid order parameter defined by $\langle b \rangle = \frac{1}{i_l - i_f}\sum_{i=i_f}^{i_l}\langle b_i \rangle$ extrapolated to infinite longitudinal size vs temperature. (a) Hard-core constraint model with $V = 0$ and filling fraction $n = 0.5$ using OBC. (b) Soft-core boson model with filling fraction $n = 1.0$ and $U/t = 6.0$ using OBC.

yields crossings for stiffnesses and BEC order parameter:

$$\rho_{S,\parallel(\perp)}(T_c) \times L^{z+d-2}, \tag{26}$$

with $d = 3$, $z = 0$ for a thermal transition, and

$$\rho_0(T_c) \times L^{2\beta/\nu}, \tag{27}$$

where $\beta = 0.3486$ and $\nu = 0.6717$ are the critical exponents of the 3D XY universality class [36,37]. From the results given in Fig. 4 the three crossings are in perfect agreement, giving for $V = 0$ a critical temperature $T_c/t = 0.323(1)$. Compared to the critical temperature from our MPS + MF approach of $T_c/t \approx 0.4$ we find that the difference is significantly better than a factor of 2 [38].

The soft-core model finite temperature data is computed for $U/t = 6.0$ since leaving U too small makes the local Hilbert space truncation increasingly erroneous. A notable feature is the increased critical temperature at around $T_c/t \approx 0.95$ as seen in Fig. 3(b), which puts these transitions squarely within the range of being observable within current experiments.

2. T_c dependence on $t_\perp$

The dependency of $\langle b \rangle$ on T does not change qualitatively with $t_\perp$, but the value of T_c does scale with $t_\perp$, as shown in Fig. 5. Combining bosonization and mean field theory this scaling has been obtained as $T_c \sim t_\perp^{\frac{2}{3}}$ for this system [22]. Thus, we have performed a fit to the data with a power law given by

$$T_c = c_1 t_\perp^{c_2}. \tag{28}$$

In Fig. 5(a) we perform a power-law fit of our data and obtain the exponent $c_2 \approx 0.628$. The scaling disagrees somewhat with the analytical value of $c_2 = 2/3$. This is expected as the analytical value is less accurate for larger T_c. Further, we find the QMC T_c scaling, $c_2 \approx 0.629$, by fitting to all data points in the same manner. We do not expect the scaling to agree with the analytical expression which relies on mean-field theory—see Sec. V for a discussion of the different scaling behaviors.

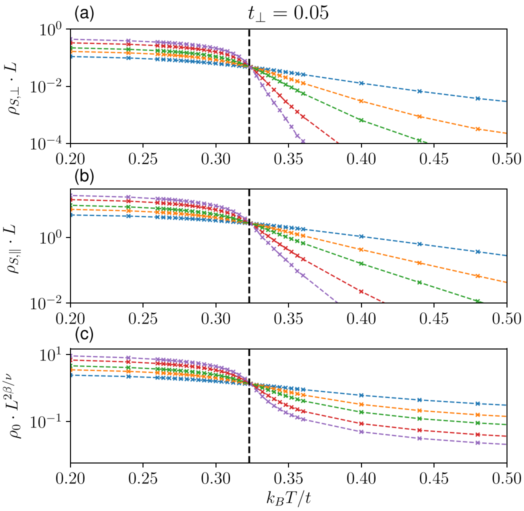

FIG. 4. Finite temperature QMC data for the full 3D model Eq. (1) at $V = 0$ indicating a transition at $T_c/t = 0.323(1)$ using (a) the transverse superfluid stiffness $\rho_{S,\perp}$ scaled with L, (b) the longitudinal superfluid stiffness $\rho_{S,\parallel}$ scaled with L, (c) the condensate density ρ_0 scaled with $L^{2\beta/\nu}$ (see text).

Using the same approach it is also possible to produce an analytical expression for the critical temperature [22]:

$$T_c = \frac{v_s n}{4\pi}\left[F(K)\frac{t_\perp z_c}{v_s n}\right]^{\frac{2K}{4K-1}}, \tag{29}$$

where K, v_s are the Tomonoga-Luttinger liquid (TLL) parameters [19], n is the density, and z_c the coordination number. The function F is given by

$$F(K) = A_B(K)\sin\left(\frac{\pi}{4K}\right)\beta^2\left(\frac{1}{8K}, 1 - \frac{1}{4K}\right), \tag{30}$$

where the amplitude $A_B(K)$, relating the microscopic lattice operators to the ones of the effective field theory, is nonuniversal and depends on the specifics of the model, and $\beta(x, y)$ is the Euler beta function. Within the mean-field approximation, Eq. (29) is exact and fit free, as long as K, v_s, and A_B are known. Hence, using ground-state DMRG we can obtain these three parameters from numerical fitting of the single particle density matrix [19] at $T = 0$. Thus, it is possible to produce critical temperatures given a ground-state calculation of a 1D system with conserved quantum numbers which is considerably less costly computationally. These values will be good approximations as long at T_c is only a small fraction of the systems bandwidth—the deviations between Eq. (29) and our MPS + MF numerics at larger T_c values visible in Fig. 5(a) are due to this. Conversely, at small T_c the agreement is excellent.

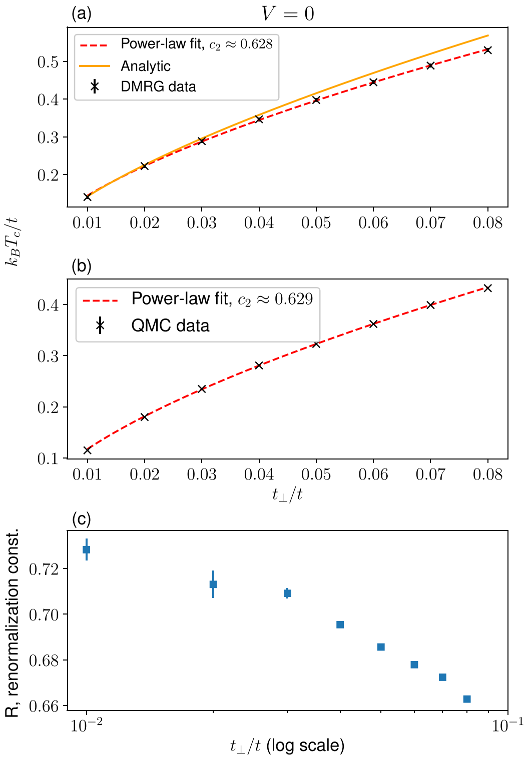

FIG. 5. The critical temperature T_c of hard-core bosons at $V = 0$ and $n = 0.5$ vs the transverse hopping $t_\perp$. (a) The red dashed line is a power-law fit to the data points (black crosses). The orange solid line is an analytical computation of T_c based on Eq. (29). (b) A power-law fit to the QMC T_c data. (c) The constant R from Eq. (31) so that the QMC T_c fits the analytical expression.

It is possible to extract critical temperature dependence on $t_\perp$ from QMC as well, and the results are shown in Fig. 5(b). Using the analytical expression Eq. (29) with a renormalization of $t_\perp$ allows the overlapping of QMC data and analytical data [39]:

$$T_c = \frac{v_s n}{4\pi}\left[F(K)\frac{R \cdot t_\perp z_c}{v_s n}\right]^{\frac{2K}{4K-1}}, \tag{31}$$

where the renormalization constant $R \in [0.74, 0.66]$, depending on $t_\perp$, is found to fit the QMC data as shown in Fig. 5(c). This renormalization constant has been discussed in the literature extensively [5,39–44], but here we find that as $t_\perp$ decreases, it appears to converge to a larger value than the one found in Ref. [39] for the case of an $SU(2)$-invariant system.

3. T_c dependence on V

The data presented so far for finite temperature have been in the simplified regime of no nearest-neighbor repulsion $V = 0$. However, the MPS + MF algorithm garners none or slight penalties in having finite V. This yields the possibility of measuring how the critical temperature depends on repulsive interactions. Further, it is interesting to see whether the relation between T_c estimates from QMC and MPS + MF remains the same when interactions are turned on.

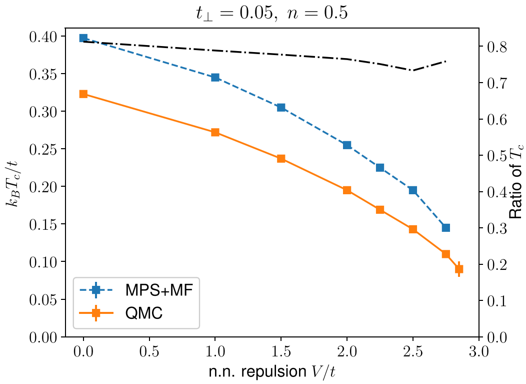

FIG. 6. A plot of the critical temperature from superfluid to normal phase. The blue dashed line is computed using MPS + MF with OBC and the orange solid line using QMC. The black dash-dotted line is a ratio of the two results with values on the right axis.

In general, when repulsive interactions are turned on we know from Fig. 2 that the superfluid should weaken. We expect that the critical temperature is depressed for stronger interactions and this can be seen in Fig. 6. Remarkably, the ratio of critical temperatures is confined to a narrow band

$$0.73 < \frac{T_c^{\mathrm{QMC}}}{T_c^{\mathrm{MPS+MF}}} < 0.82. \tag{32}$$

This remains true even when the quantum critical point at $V_c/t \approx 3$ is approached.

We point out that the MPS + MF approach we have developed here has a crucial advantage over the TLL + MF framework behind Eq. (29): It can compute T_c even in regimes where the individual 1D systems no longer realize a TLL, such as for $V/t > 2$ for HCBs and $U/t > 3.3$ for SCBs, as shown in Figs. 3(b) and 6.

V. DISCUSSION

The zero-temperature SF-CDW transition is an example of so-called dimensional crossover [21]. We can see this by noting that the order parameter for SF witnesses an exchange of bosons between chains. When the order parameter for SF goes to zero tunneling between chains is completely suppressed. The system now behaves more like a set of 1D systems with a remnant of interchain coupling only QMC can still resolve, whereas in the case of finite SF order parameter the exchange of particles made the system fully 3D. So, the crossover from 3D to 1D becomes especially pronounced around the transition point. A major difference to the quantum phase transitions from SF to CDW occurring in 3D systems with isotropic tunneling and interactions that we are showing here is that the transition in the present quasi-1D systems is not second order but first order for HCBs (see Appendix D), and possibly also for SCBs, as discussed below.

At the same time, it is evident from Fig. 2 that soft-core and hard-core bosons have qualitatively similar behavior. One notable difference is that the charge gap is much larger in the soft-core case. This is likely due to the transitions occurring at much larger values of U. Thus, the energy penalty for adding and removing particles is much larger than in the hard-core case. In addition, there is a small region around the transition where the two order parameters coexist, i.e., where both are small but finite. But as the limitations of mean-field approaches (of which we are using a partial one) in predicting supersolids are well documented, we refrain from concluding the existence of such a state here. We also note that the SF order parameter is enhanced for the soft-core case. This could be explained by the fact that sites are almost never locked as they often would be in the hard-core case. In other words, it is almost always possible to inject particles into the system in contrast to the hard-core case. If the maximum boson number is reached the site is artificially locked but the amplitude for a state where this occurs is negligible in accordance with Eq. (2).

For soft-core bosons, in the true 1D case the CDW transition occurs at $U_{\mathrm{1D}}/t \approx 3.3$ [34] whereas in the quasi-1D case with $t_{\perp}/t = 0.05$ (see Fig. 2) it does not occur until $U_{\mathrm{Q1D}}/t \approx 8.12$ [45]. For comparison, a 3D system with isotropic tunneling yields $U_{\mathrm{3D}}/t = 29.94(2)$ [46] indicating that the large increase we observe from U_{1D} to U_{Q1D} is reliable and the value of U_{Q1D} is heavily dependent on $t_{\perp}$.

Overall, the soft-core boson case appears to differ qualitatively from the hard-core case when it comes to transition order. In the soft-core model we could not find any clear first order behavior in the superfluid order parameter while the charge gap behaves similarly to the hard-core case—in fact, charge gaps in both cases show a more pronounced discontinuity than the supefluid order parameter or the transverse superfluid stiffness (see Fig. 2). While we cannot detect a jump in the SF order parameter, and thus a full first-order transition, for the SCB system, this scenario remains the most likely explanation for the observed behavior. We note that there may be effects of the mean-field approximation that degrade any jump below the threshold that we could numerically resolve. The only other alternative we see that could explain the behavior of Fig. 2 is that of a simultaneous SF and CDW order, i.e., a supersolid. As discussed above, it appears to us that such an alternative would however require more evidence than what can be supplied with the MPS + MF approach on its own.

For the critical temperatures of the SF to normal transition, the analytical prediction agrees well with the numerical correspondents as seen in Fig. 5, especially at low T_c's. It is notable that the scaling of both MPS + MF and QMC data are very similar, another positive for the approximative MPS + MF approach, with a power below that of the power of $2/3$ predicted from TLL + MF. At small $t_{\perp}$ we expect and find improved agreement between analytical theory and MPS + MF, in line with the fact that the TLL + MF prediction will work better as T_c becomes a small fraction of the systems bandwidth. For both the MPS + MF and the QMC data we find that increasingly constraining the fitting window to the smallest values of $t_{\perp}$ yields exponents approaching $c_2 \approx 2/3$ from below, showing that the mean-field approximation becomes better with decreasing $t_{\perp}$. The close agreement in the scaling behavior of T_c with $t_{\perp}$ between the QMC and MPS + MF techniques, and their common disagreement with the $t_{\perp}^{2/3}$-scaling derived from TLL + MF points to the source being within the TLL approximation of the microscopic lattice Hamiltonian of the chains.

For the temperature data at finite repulsion in a hard-core system it is interesting to note the relative constancy of the T_c ratio between MPS + MF and QMC. The different critical temperatures seem to agree less for larger values of repulsion with the exception of the point at $V = 2.75$ where there is a different trend.

While the results between QMC and MPS + MF differ somewhat we note the differing efficiency of the two algorithms. QMC data in this paper have been obtained using 30 000 equilibration steps and 1 000 000 measurement steps. For a single core [Intel(R) Xeon(R) Gold 6140 CPU @ 2.30 GHz] we find that

(i) CPU time for equilibration $\approx 0.001L^4$ sec,
(ii) CPU time for measurements $\approx 0.1L^4$ sec.

For MPS + MF we note that scaling is exactly that of typical DMRG:

$$t_{\mathrm{tot}} \sim N_{\mathrm{sol}} d^2 \chi^3 L, \tag{33}$$

where d is the local Hilbert space dimension, χ is the bond dimension, and L the system size. The MPS + MF routine has the added complication of having to perform several DMRG calculations. We have found that the number of required solutions N_{sol} vary greatly, particularly close to transitions. Deep in an ordered phase the number of required solutions can be as low as $N_{\mathrm{sol}} \sim 5$. Close to a phase transition we find this number able to reach $N_{\mathrm{sol}} \sim 50$ for OBC and $N_{\mathrm{sol}} \sim 30$ for PBC including the various guessing heuristics we employ as mentioned in Sec. III. Most important is that N_{sol} is not very dependent on system size, approximately conserving the L dependence of Eq. (33).

We compare data using a PBC model, and the efficiency should be compared between these two cases as well. Note that using OBC gives an incredible boost to efficiency due to the lower bond dimension, which can be used for the finite temperature case. It is further worthwhile to note that QMC would obtain a better scaling with system size for finite temperature and thus shorter run times as well.

On an [Intel(R) Xeon(R) Processor E5-2630 v4 CPU @ 2.20 GHz] we find an $L = 60$ system running for ≈ 1600 seconds per solution in MPS + MF. With the largest number of loops at $N_{\mathrm{sol}} \sim 30$ we arrive at

(i) QMC time: 15 days,
(ii) MPS + MF: 0.55 days.

As expected the MPS + MF algorithm ends up comparing well when doing single-core calculations. It is worthwhile to mention that QMC can scale up its measurement phase to several cores where calculation speed increases linearly with each core added. The degree with which MPS-based codes can exploit parallelism varies widely by implementation, but linear speedups in the number of CPU cores are generally not available over as wide a range as for QMC. Nevertheless, scientific projects typically address some finite area of parameter space, meaning that the MPS + MF can obviously exploit perfect (and trivial) parallelism in system parameters.

VI. CONCLUSION

Our results show that an approach using DMRG to solve a decoupled 3D system self-consistently is valid for use on an anisotropic system and also reproduces the transition points with reasonable accuracy. In particular, the SF to CDW phase transition has nearly equal critical repulsion V_c for the MPS + MF case compared to QMC. The major benefit is that the DMRG approach is computationally cheaper than the corresponding exact QMC. We will further be able to simulate real-time dynamics on the states produced by this framework of MPS + MF. For the finite temperature transition to a normal phase the critical temperature deviates more from the exact case. However, this deviation is much less sizable than what a full mean-field approximation produces. This method presents a powerful possibility of treating anisotropic 2D and 3D systems quickly using DMRG, in particular beyond the TLL approach.

Another key finding of this work is the first-order nature of the quantum phase transition between the superfluid and the charge density wave order for hard-core bosons in these quasi-1D anisotropic systems, as opposed to the expected purely second order transition in a 3D system isotropic in tunneling (and interactions, in the case of HCBs). At the same time, the discontinuous opening of the charge gap contra the apparent continuous vanishing of the SF order parameter, which occurs for the case of soft-core bosons, may indicate different orders of the transition in that specific system. The former suggesting first order while the latter looks like second order. Our current method and analysis is insufficient to determine whether there is a very small jump. If that is the case it is further possible that the gap gets smoothed out by the mean-field treatment. A more detailed analysis of the soft-core model is required to ascertain whether the transition is truly first order.

The method presented in this paper reproduces previous analytical results. Critical temperature calculations using this method scale with transverse hopping strength $t_\perp$ corresponding to what you would obtain using an effective field theory on the 3D system and then decoupling with mean-field theory. Replacing the effective field theory with DMRG we find similar scaling laws with a modified exponent. In addition, using ground state data from the normal 1D MPS routine we may produce a critical temperature estimate from the field theory. Both the scaling and estimated value agree well with the presented approach at small $t_\perp$, where agreement is expected. The reasonably close agreement to theory allows us to trust our numerical methods in the context of mean-field theory. Combining analytical and numerical methods in this manner could allow us to obtain T_c estimates in parameter regions that are too computationally costly. This will be especially true for an extension of our method to fermionic systems, where, even putting aside the sign problem, auxiliary-field QMC approaches scale much worse in the number of lattice sites than in QMC for bosons (cubic vs linear scaling).

ACKNOWLEDGMENTS

We would like to thank Thierry Giamarchi, Thomas Köhler, and Shintaro Takayoshi for useful discussions. This work has received funding through an ERC Starting Grant from the European Union's Horizon 2020 research and innovation programme under Grant agreement No. 758935. Part of the simulations were performed using the MPToolkit, written by Ian McCulloch [47]. The computations were performed on resources provided by SNIC through Uppsala Multidisciplinary Center for Advanced Computational Science (UPPMAX) under Projects SNIC 2019/3-323, SNIC 2019/8-26, SNIC 2020/1-48, SNIC 2019/35-16, uppstore2019070, and SNIC 2020/16-92. N.L. thanks the French National Research Agency (ANR) for support under project THERMOLOC ANR-16-CE30-0023-0. We acknowledge CALMIP (Grants No. 2018-P0677 and 2019-P0677) and GENCI (Grant No. A0030500225) for high-performance computing resources.

APPENDIX A: OBC BOUNDARY CONTAMINATION

When using OBC the boundaries are dissimilar from other sites in the system in that they are missing one neighboring site. Depending on the Hamiltonian this causes a bias towards either holes or particles to occupy the edge sites.

The usual method to deal with this bias is to focus on the central part of the system and assume that boundary effects do not reach in beyond a certain point. However, as can be seen from Fig. 7, the assumption does not hold for the case of the Hamiltonian in Eq. (4).

Instead we see the boundaries start a pattern of alternating particles and holes. Since it is clearly preferable to have particles on the edges in the considered system, the two edges have large weight on the occupation state. After $V/t = 3$ the pattern becomes increasingly apparent and finally the average simply does not attain the system center value. Further, even if the average was a good measure of the center value it can be seen from Fig. 7 that the boundaries actually incur a finite superfluid order inside the system which leads to a transition occurring only at $V_c/t = 3.24$.

It is further clear that this is a boundary effect since when system size is increased above the sizes used in this paper the finite size trend changes, making extrapolations difficult. In practice, to overcome the boundary effect on superfluid order in the hard-core system with nearest neighbor interaction we find that sizes of $L = 200$ are insufficiently long to see any convergence. This clearly shows the periodic boundary conditions are necessary to analyze the hard-core bosons with nearest neighbor repulsion since extrapolations to infinite size suffer no trend changes at moderate sizes.

This is a much smaller problem in the case of soft-core bosons with onsite repulsion as seen in Fig. 8. We can clearly see the order parameter saturate to a specific value at the center of the system quite quickly. Further, the plateauing does not seem to be strongly affected by the onsite repulsion.

Evidently, when there is no nearest neighbor interaction the effect of the boundaries is much smaller and OBC can safely be used. Due to these observations we assume that PBC will not yield a different result than OBC and neglect to perform the costly computations soft-core bosons with PBC would

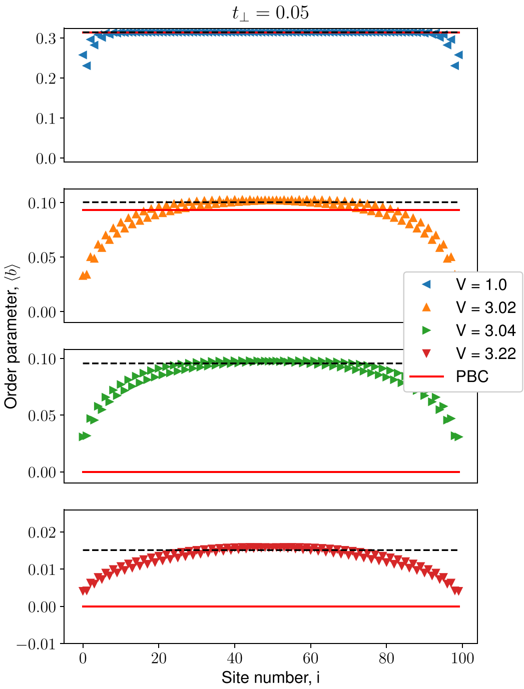

FIG. 7. Order parameter $\langle b\rangle$ across the hard-core system for different values of nearest neighbor repulsion V using OBC. The OBC data is for an $L = 100$ system and the PBC data is extrapolated to $L \to \infty$.

entail. Thus we have chosen to use PBC for the hard-core system with nearest neighbor interactions and OBC for the soft-core system with onsite interactions.

APPENDIX B: DENSITY PLATEAUS

When the considered model does not conserve particle number it is not possible to use energy differences of states with different particle number to determine the charge gap (as in, e.g., Karakonstantakis *et al.* [20]). This is because it can occur that

$$n(\mu) = n(\mu + \delta\mu), \tag{B1}$$

where $\delta\mu$ is some small shift from μ. In practice, this occurs in the CDW phase which yields a certain arbitrariness to the energy since certainly

$$E(\mu) \neq E(\mu + \delta\mu) \tag{B2}$$

as long as there are any particles in the system, while from Eq. (B1) we would obtain

$$E(N) = E(n(\mu)) = E(n(\mu + \delta\mu)). \tag{B3}$$

Another method may be used based on the variation of μ. When computing density versus chemical potential, in the CDW phase you find plateaus of constant density, as shown in Fig. 9(a), whose width are the energy required to increase particle number by one. It is possible to compute how much the chemical potential μ must be increased (decreased) to obtain an increase (decrease) in the systems density. This yields an upper and lower chemical potential for that particular density. The difference of this upper and lower bound is then the energy required to increase/decrease particle number.

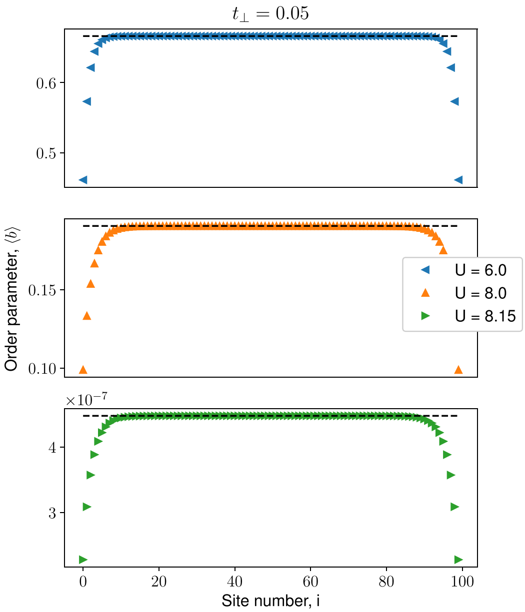

FIG. 8. Order parameter $\langle b\rangle$ across the soft-core system for different values of onsite repulsion U using OBC.

The width of the density plateau W is related to an energy difference obtained from a number-conserving calculation once you enter the CDW phase of the system

$$W \approx E(N + 1) + E(N - 1) - 2E(N). \tag{B4}$$

Further, as can be seen from Fig. 9(b), when repulsion is decreased and we enter the superfluid phase the plateauing tendency disappears. For charge gaps computed in the paper we have used a precision which is at worst $\epsilon_\mu = 1e^{-3}$ for the upper and lower limit of the plateau.

APPENDIX C: ISOTROPIC TUNNELING

The first-order nature of the transition is not entirely clear in the QMC data in Fig. 2. This is due to the fact that $t_\perp = 0.05t$ is very small. To elucidate the nature of the transition we may consider larger values of $t_\perp$ as we still expect the system to be in the same universality class.

For an isotropic case of $t_\perp = t$ the correspondent result of Figs. 2(b) and 2(c) is given in Fig. 10. Both order parameters tend to exhibit clear jumps that become sharper as system size is increased. We thus reason that the gap should remain, albeit diminished, in the case of anisotropic tunneling.

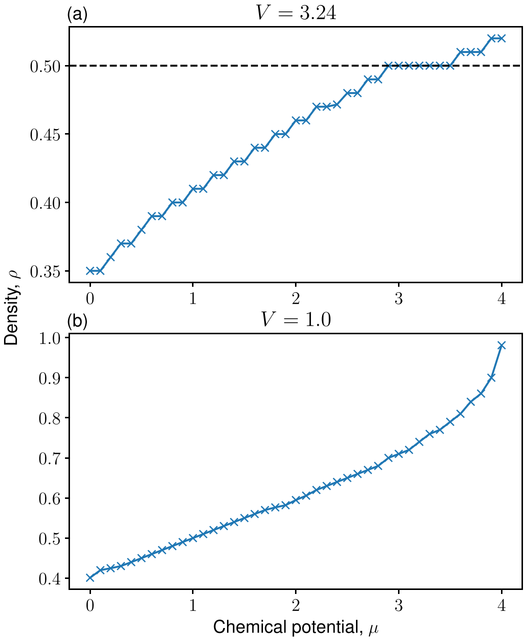

FIG. 9. Showing the density of a system with $\alpha = 0$ at a V in the (a) CDW phase and (b) the TLL phase. Note the clear plateau around $n = 0.5$ inside the CDW phase.

APPENDIX D: FIRST ORDER TRANSITION

The jump in the order parameters given by the MPS + MF routine in Fig. 2(a) and Fig. 2(c) do not by themselves guarantee first-order behavior. For the latter one of the order parameters seems to vanish continuously as far as we can resolve.

To clarify the transition order we compute additional indicators. For the soft-core case we find no issue in computing

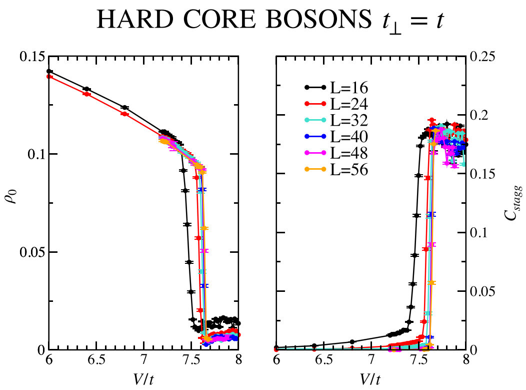

FIG. 10. BEC order parameter and CDW order parameter for the isotropic case $t_\perp = t$.

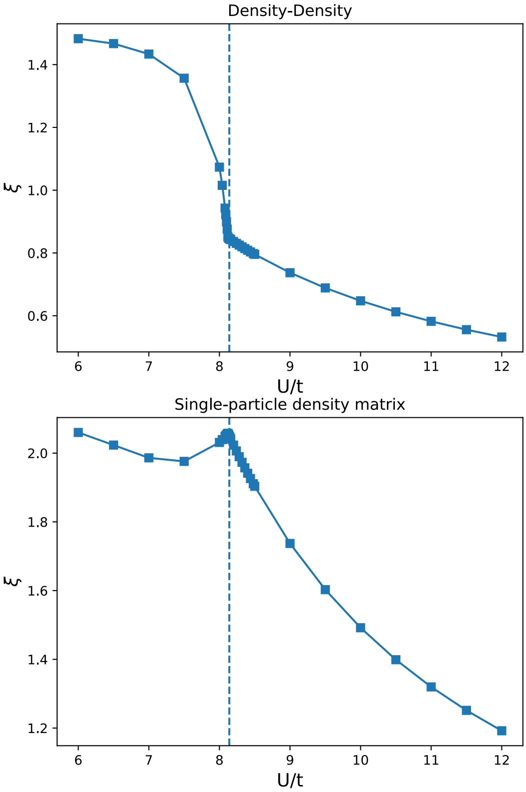

FIG. 11. Density-density correlator and single-particle density matrix vs onsite repulsion U/t in an $L = 100$ system for transverse hopping $t_\perp = 0.05t$ at bond dimension $\chi = 50$.

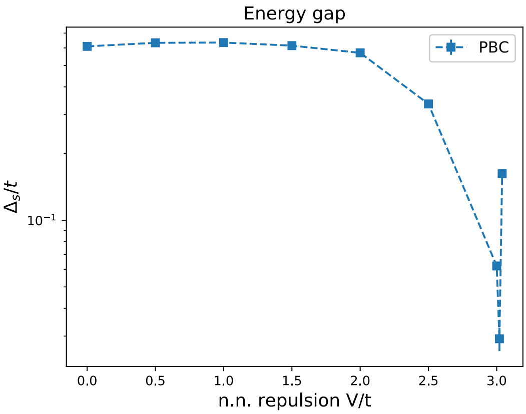

FIG. 12. Energy gaps to the first excited state extrapolated to infinity using PBC for bond dimension $\chi = 250$ with transverse hopping $t_\perp = 0.05t$.

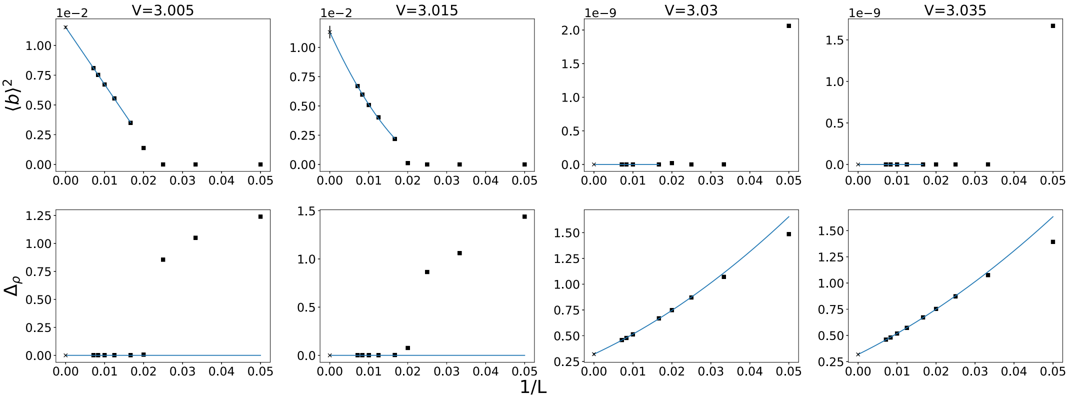

FIG. 13. Squared order parameter and charge gap vs inverted system size (black squares) for the hard-core boson model with PBC. The blue solid line is a fit following Eq. (21) for the order parameter and Eq. (19) for the charge gap.

correlation functions and obtaining correlation lengths using the scaling behavior for single-particle density matrix and density-density correlator, respectively:

$$\langle b_i^\dagger b_{i+r}\rangle \sim A_0 + B_0 \exp(-r/\xi), \tag{D1}$$

$$\langle n_i n_{i+r}\rangle \sim A_1 + B_1 \exp(-r/\xi), \tag{D2}$$

where ξ is the correlation length (differing between the two correlators).

As can be seen from Fig. 11 there is a change of trend in the correlation length at the transition. In addition, the single-particle density matrix has an increasing correlation length with a maximum at the transition. As far as we can resolve there is no divergence and no increased tendency thereof with increased bond dimension. This indicates we are capturing the correct behavior. Since the correlation length is finite all across the transition we conclude that the soft-core superfluid to charge density wave transition is first order.

For the hard-core system it is difficult to fit Eqs. (D1) and (D2) to the measured correlators. We find a nonexponential trend taking over after a short distance suggesting insufficient bond dimension for carrying the correlations over sufficient distance to obtain good fits for a correlation length.

To obtain additional proof of the transition order in this case we instead measure the (infinite size) gap to the first excited state

$$\Delta_s = \lim_{L\to\infty} E_1(L) - E_0(L). \tag{D3}$$

For a second order transition we would expect the gap to the first excited state to be unchanged across the transition.

As can be seen from Fig. 12 the gap defined by Eq. (D3) jumps by an order of magnitude across the transition and changes direction abruptly. We take this to indicate a first order transition since the gap to the excited state is not changing smoothly over the transition. Together with the jumplike behavior of both the SF and CDW order parameter in Fig. 2(a) we conclude that the hard-core transition is first order as well.

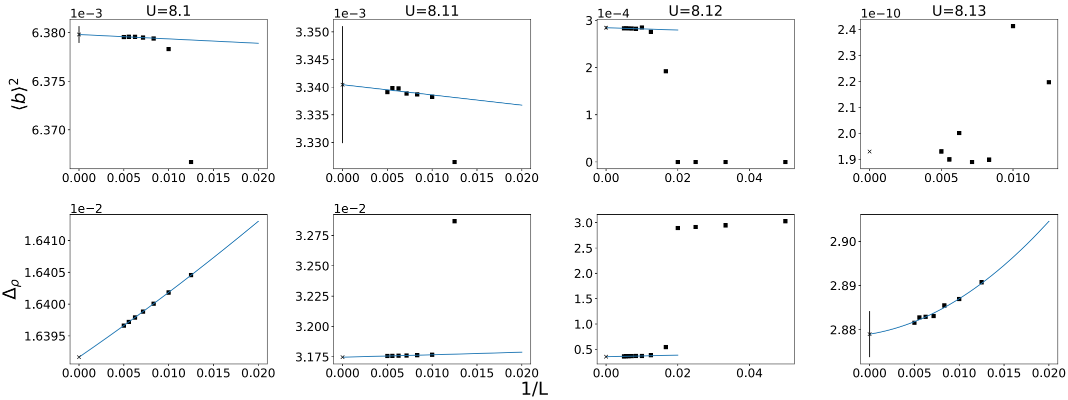

FIG. 14. Squared order parameter and charge gap vs inverted system size (black squares) for the soft-core boson model with OBC. The blue solid line is a fit following Eq. (21) for the order parameter and Eq. (19) for the charge gap.

APPENDIX E: FINITE-SIZE EXTRAPOLATION

We present the finite size data which after extrapolation yields the data given by MPS + MF in Figs. 2(a) and 2(d). The finite size data has been computed for a varying range of sizes depending on when a clear trend which could be extrapolated appeared. Results for the hard-core model are shown in Fig. 13. Notably, on the superfluid side order parameter increases with size. In addition, there is a certain size at which the system no longer supports superfluidity (e.g., $L = 40$ for n.n. repulsion $V = 3.005$). With increasing repulsion larger sizes are required to obtain superfluidity. We find that after $V = 3.02$ no sizes manage to obtain superfluidity and all order parameters are zero.

For the charge gap similar conditions hold. We find that below transition smaller sizes obtain a finite charge gap whereas in larger systems it is consistently zero valued. This comes as no surprise since when superfluidity fails the system is truly 1D and should follow such physics. In this case, a truly 1D system at these parameters transitions to a CDW phase at $V = 2$ and we find the expected charge gaps at sizes where superfluidity disappears.

For the soft-core case results look somewhat different as shown in Fig. 14. This is mainly due to OBC allowing us access to much larger system sizes such that only systems with finite order parameter have been considered on the superfluid side. We note that the order parameter seems to obtain large fitting errors. In relation to the size of the order parameter these errors typically remain on the order of marker size and are included in Fig. 2(d).

For the charge gap we note that it looks finite before transition. This is within the error produced by our charge gap routine as outlined in Appendix B and we consider these charge gaps zero valued. At onsite repulsion $U = 8.12$ we find the curious case of simultaneous finite (but small) charge gap and order parameter despite extrapolation which is discussed in Sec. V.

[1] M. Klanjsek, H. Mayaffre, C. Berthier, M. Horvatić, B. Chiari, O. Piovesana, P. Bouillot, C. Kollath, E. Orignac, R. Citro, and T. Giamarchi, Phys. Rev. Lett. **101**, 137207 (2008).

[2] P. Bouillot, C. Kollath, A. M. Läuchli, M. Zvonarev, B. Thielemann, C. Rüegg, E. Orignac, R. Citro, M. Klanjšek, C. Berthier, M. Horvatić, and T. Giamarchi, Phys. Rev. B **83**, 054407 (2011).

[3] C. Rüegg, K. Kiefer, B. Thielemann, D. F. McMorrow, V. Zapf, B. Normand, M. B. Zvonarev, P. Bouillot, C. Kollath, T. Giamarchi, S. Capponi, D. Poilblanc, D. Biner, and K. W. Krämer, Phys. Rev. Lett. **101**, 247202 (2008).

[4] M. Jeong, H. Mayaffre, C. Berthier, D. Schmidiger, A. Zheludev, and M. Horvatić, Phys. Rev. Lett. **111**, 106404 (2013).

[5] R. Blinder, M. Dupont, S. Mukhopadhyay, M. S. Grbić, N. Laflorencie, S. Capponi, H. Mayaffre, C. Berthier, A. Paduan-Filho, and M. Horvatić, Phys. Rev. B **95**, 020404(R) (2017).

[6] A. Schwartz, M. Dressel, G. Grüner, V. Vescoli, L. Degiorgi, and T. Giamarchi, Phys. Rev. B **58**, 1261 (1998).

[7] T. Giamarchi, Chem. Rev. **104**, 5037 (2004).

[8] C. Bourbonnais and D. Jérome, in *The Physics of Organic Superconductors and Conductors*, edited by A. Lebed (Springer, New York, 2007), p. 358.

[9] D. Jérome and S. Yonezawa, C. R. Phys. **17**, 357 (2016).

[10] A. Kantian, M. Dolfi, M. Troyer, and T. Giamarchi, Phys. Rev. B **100**, 075138 (2019).

[11] T. Nagata, M. Uehara, J. Goto, J. Akimitsu, N. Motoyama, H. Eisaki, S. Uchida, H. Takahashi, T. Nakanishi, and N. Môri, Phys. Rev. Lett. **81**, 1090 (1998).

[12] E. Dagotto, Rep. Prog. Phys. **62**, 1525 (1999).

[13] J.-K. Bao, J.-Y. Liu, C.-W. Ma, Z.-H. Meng, Z.-T. Tang, Y.-L. Sun, H.-F. Zhai, H. Jiang, H. Bai, C.-M. Feng, Z.-A. Xu, and G.-H. Cao, Phys. Rev. X **5**, 011013 (2015).

[14] M. D. Watson, Y. Feng, C. W. Nicholson, C. Monney, J. M. Riley, H. Iwasawa, K. Refson, V. Sacksteder, D. T. Adroja, J. Zhao, and M. Hoesch, Phys. Rev. Lett. **118**, 097002 (2017).

[15] D. Jérome, A. Mazaud, M. Ribault, and K. Bechgaard, J. Phys. Lett. **41**, 95 (1980).

[16] T. Giamarchi and A. M. Tsvelik, Phys. Rev. B **59**, 11398 (1999).

[17] M. Jeong, H. Mayaffre, C. Berthier, D. Schmidiger, A. Zheludev, and M. Horvatić, Phys. Rev. Lett. **118**, 167206 (2017).

[18] M. Dupont, S. Capponi, N. Laflorencie, and E. Orignac, Phys. Rev. B **98**, 094403 (2018).

[19] T. Giamarchi, *Quantum Physics in One Dimension*, 1st ed. (Oxford University Press, New York, 2003), p. 448.

[20] G. Karakonstantakis, E. Berg, S. R. White, and S. A. Kivelson, Phys. Rev. B: Condens. Matter Mater. Phys. **83**, 054508 (2011).

[21] A. F. Ho, M. A. Cazalilla, and T. Giamarchi, Phys. Rev. Lett. **92**, 130405 (2004).

[22] M. A. Cazalilla, A. F. Ho, and T. Giamarchi, New J. Phys. **8**, 158 (2006).

[23] A. Frisch, M. Mark, K. Aikawa, S. Baier, R. Grimm, A. Petrov, S. Kotochigova, G. Quéméner, M. Lepers, O. Dulieu, and F. Ferlaino, Phys. Rev. Lett. **115**, 203201 (2015).

[24] S. Baier, D. Petter, J. H. Becher, A. Patscheider, G. Natale, L. Chomaz, M. J. Mark, and F. Ferlaino, Phys. Rev. Lett. **121**, 093602 (2018).

[25] S. R. White, Phys. Rev. Lett. **69**, 2863 (1992).

[26] U. Schollwöck, Ann. Phys. **326**, 96 (2011).

[27] O. F. Syljuasen and A. W. Sandvik, Phys. Rev. E **66**, 046701 (2002).

[28] S. R. White, Phys. Rev. B **72**, 180403(R) (2005).

[29] M. E. Fisher, Phys. Rev. A **8**, 1111 (1973).

[30] E. L. Pollock and D. M. Ceperley, Phys. Rev. B **36**, 8343 (1987).

[31] A. W. Sandvik, Phys. Rev. B **56**, 11678 (1997).

[32] N. Laflorencie, S. Capponi, and E. Sorensen, Eur. Phys. J. B **24**, 77 (2001).

[33] I. Bloch, J. Dalibard, and W. Zwerger, Rev. Mod. Phys. **80**, 885 (2008).

[34] K. V. Krutitsky, Phys. Rep. **607**, 1 (2016).

[35] J. Carrasquilla and M. Rigol, Phys. Rev. A **86**, 043629 (2012).

[36] E. Burovski, J. Machta, N. Prokof'ev, and B. Svistunov, Phys. Rev. B **74**, 132502 (2006).

[37] M. Campostrini, M. Hasenbusch, A. Pelissetto, and E. Vicari, Phys. Rev. B **74**, 144506 (2006).

[38] M. Rigol and A. Muramatsu, Comput. Phys. Commun. **169**, 416 (2005).

[39] C. Yasuda, S. Todo, K. Hukushima, F. Alet, M. Keller, M. Troyer, and H. Takayama, Phys. Rev. Lett. **94**, 217201 (2005).

[40] V. Y. Irkhin and A. A. Katanin, Phys. Rev. B **61**, 6757 (2000).

[41] A. Praz, C. Mudry, and M. B. Hastings, Phys. Rev. B **74**, 184407 (2006).

[42] D. X. Yao and A. W. Sandvik, Phys. Rev. B **75**, 052411 (2007).

[43] B. Thielemann, C. Rüegg, K. Kiefer, H. M. Ronnow, B. Normand, P. Bouillot, C. Kollath, E. Orignac, R. Citro, T. Giamarchi, A. M. Läuchli, D. Biner, K. W. Krämer, F. Wolff-Fabris, V. S. Zapf, M. Jaime, J. Stahn, N. B. Christensen, B. Grenier, D. F. McMorrow, and J. Mesot, Phys. Rev. B **79**, 020408(R) (2009).

[44] S. C. Furuya, M. Dupont, S. Capponi, N. Laflorencie, and T. Giamarchi, Phys. Rev. B **94**, 144403 (2016).

[45] T. D. Kühner, S. R. White, and H. Monien, Phys. Rev. B **61**, 12474 (2000).

[46] B. Capogrosso-Sansone, N. V. Prokof'ev, and B. V. Svistunov, Phys. Rev. B **75**, 134302 (2007).

[47] I. P. McCulloch, Matrix Product Toolkit, https://people.smp.uq.edu.au/IanMcCulloch/mptoolkit/index.php.